REAL-TIME IMPEDIMETRIC MICROFLUIDIC DROPLET MEASUREMENT: IDM

A THESIS SUBMITTED TO
THE GRADUATE SCHOOL OF ENGINEERING AND SCIENCE
OF BILKENT UNIVERSITY
IN PARTIAL FULFILLMENT OF THE REQUIREMENTS FOR
THE DEGREE OF
MASTER OF SCIENCE
IN
MATERIALS SCIENCE AND NANOTECHNOLOGY

By
Abtin Saateh
August 2019

Real-time Impedimetric Microfluidic Droplet Measurement: iDM
By Abtin Saateh
August 2019

We certify that we have read this thesis and that in our opinion it is fully adequate, in scope and in quality, as a thesis for the degree of Master of Science.

Çağlar Elbüken(Advisor)

Barbaros Çetin

Ender Yıldırım

Approved for the Graduate School of Engineering and Science:

Ezhan Karaşan
Director of the Graduate School

ABSTRACT

REAL-TIME IMPEDIMETRIC MICROFLUIDIC DROPLET MEASUREMENT: IDM

Abtin Saateh
M.S. in Materials Science and Nanotechnology
Advisor: Çağlar Elbüken
August 2019

Droplet-based microfluidic systems require a precise control on droplet physical properties, hence measuring the morphological properties of droplets is critical to obtain high sensitivity analysis. The ability to perform such measurements in real-time is another demand which has not been addressed yet. In this study, coplanar electrodes were used, and configured in differential measurement mode for impedimetric measurement of size and velocity. To obtain the size of the droplets, detailed 3D finite element simulations of the system were performed. The interaction of the non-uniform electric field and the droplet was investigated. The electrode geometry optimization steps were described and design guideline rules were laid out. Size of the electrodes was optimized based on the simulations for droplet lengths ranging from 300 to 1500 µm. A user-friendly software was developed for real-time observation of droplet length and velocity together with in-situ statistical analysis results. A detailed comparison between impedimetric and optical measurement tools is given. Finally, to illustrate the benefit of having real-time analysis, iDM was used for experimental studies. First study case is the response time of the syringe pump and pressure pump driven droplet generation devices. This analysis allows one to evaluate the 'warm-up' time for a droplet generator system after which droplets reach the desired stead-state size required by the assay of interest. Second, an evaluation chip was designed to investigate effective factors and their interplay with droplet length variation. A comprehensive design of experiment (DoE) method is utilized. Analyzing the obtained results revealed effect of each factor and their interactions. Exploiting results of this study contributes to monodisperse microfluidic droplet generation. Monodisperse polymeric particles of polyethylene glycol were synthesized to demonstrate the potentials of monodisperse droplet generation in biochemical synthesis/analysis.

Keywords: Droplet microfluidics, Real-time, Droplet measurement, Impedimetric, Label-free, Droplet Monodispersity.

ÖZET

GERÇEK ZAMANLI İMPEDİMETRIK MİKROAKIŞKAN DAMLACIK ÖLÇÜMÜ: IDM

Abtin Saateh
Malzeme Bilimi ve Nanoteknoloji, Yüksek Lisans
Tez Danışmanı: Çağlar Elbüken
Ağustos 2019

Damlacık temelli mikroakışkan sistemler, damlacık fiziksel özellikleri üzerinde kesin bir kontrol gerektirir. Bu yüzden, yüksek hassasiyetli analiz elde etmek için, damlacıkların morfolojik özelliklerinin ölçümü kritik bir öneme sahiptir. Böylesi ölçümleri gerçek zamanlı gerçekleştirebilme yetisi, daha önce üzerinde durulmamış diğer bir özelliktir. Bu çalışmada, boyut ve hızın impedimetrik ölçümü için farklı ölçüm modlarında düzlemsel elektrotlar kullanılmıştır. Damlacıkların boyutunu elde etmek için, sistemin detaylı 3 boyutlu sonlu eleman analizi gerçekleştirilmiştir. Homojen olmayan elektrik alan ile damlacıkların etkileşimi araştırılmıştır. Elektrot geometri optimizasyon adımları tanımlanmış ve tasarım kuralları ortaya konmuştur. 300 - 1500 µm uzunluktaki damlacıklar için yapılan simülasyonlara dayanarak elektrot boyutları optimize edilmiştir. Anlık istatistiksel analiz sonuçlarıyla birlikte damlacıkların uzunluk ve hızlarının gerçek zamanlı incelenmesi için, kullanıcı dostu bir bilgisayar uygulaması geliştirilmiştir. İmpedimetrik ve optiksel ölçüm gereçlerinin detaylı bir karşılaştırması yapılmıştır. Son olarak, gerçek zamanlı analize sahip olmanın faydalarını göstermek açısından, deneysel çalışmalar için iDM kullanılmıştır. Birinci çalışma, şırınga ve basınç pompa kullanan damlacık oluşturma cihazlarının yanıt zamanlarıdır. Bu analiz, kullanıcının damlacık oluşturma sistemlerindeki ısınma zamanının değerlendirmesini olanaklı kılar ki bu zamanı takiben damlacıklar testlerde gereksinim duyulan kararlı hal boyutuna ulaşırlar. İkincil olarak, damlacık uzunluk değişimleriyle birlikte, etkin faktörlerin ve bunların etkileşiminin araştırılması için bir değerlendirme çipi geliştirilmiştir. Detaylı bir deney tasarım metodu kullanılmıştır. Elde edilen sonuçların analizi, her faktörün ve bunların etkileşiminin etkisini ortaya çıkarmıştır. Bu çalışmadaki sonuçlar, eş dağılımlı mikroakışkan damlacık oluşumuna katkı sunmaktadır. Eş dağılımlı damlacık üretiminin potansiyelini biyokimyasal sentez/analiz ler de göstermek için, eş dağılımlı polietilen glikol polimer parçacıkları sentezlenmiştir.

Anahtar sözcükler: Mikroakışkan Damlacık, Gerçek Zamanlı, İmpedimetrik, Etiketsiz, Damlacık Eş Dağılımı.

Acknowledgement

First and foremost, I would like to express my deepest gratitude to my advisor, Dr. Çağlar Elbüken who gave me the opportunity to work in an exceptional research environment. I know him, for his support, guidance, and encouragement over my masters; and more importantly, for what I learned beyond the academia, the life lessons and professional attitude which will remain with me throughout my life. Thanks for your scientific guidance and above all your friendship. I would like to appreciate Dr. Bülend Ortaç for his pieces of advice throughout my research work and education, especially with the laboratory facilities.

I would like to thank the members of my thesis committee Dr. Barbaros Çetin from Bilkent University, and Dr. Ender Yıldırım from Çankaya University for their insightful comments and feedback.

My whole accomplishments belong to my great, kind family that has constantly supported me in every aspect, though from hundreds of kilometers away. For a devoted love, distance never matters.

My heart goes out to my beloved grandfather, whom I lost during my thesis work without having the opportunity of saying the last goodbye to him. It is hard to accept the absence and I will miss you forever.

I am grateful to be a team member of Elbüken Lab and collaborate with such nice people. In particular, I would like to thank Ali Kalantarifard, Pınar Beyazkılıç and Murat Serhatlıoğlu for their scientific advices, many insightful discussions and suggestions. Their assistance in research and conducting experiments taught me a lot. I want to thank Ziya Işıksaçan for all his support and nice chats. Also, thanks to Oğuz Tolga Çelik for his assistance in this project. Finally, I want to thank all my current and former colleagues those who have crossed my path and have left a mark during this journey.

It is my pleasure to have the company of the kind, my friends and colleagues. I would like to thank Melis Özkan, Nuray Gündüz, Begimai Adilbekova, Çisil

Köksaldı, Merve Üstünçelik, Ehsan Yousefi, Sasan Salmani Pour Avval, Mahyar Ghavami, Ilkin Mammadov, Şahmurat Kazak, Doğu Özyiğit, and Hüseyin Can Çamiçi for the all unforgettable memories that they have created for me beyond reckoning. You will stay in my heart forever.

Contents

List of Figures

List of Tables

Chapter 1

Introduction

This chapter provides a brief review on microfluidic systems, specifically on droplet microfluidics and detection systems currently in use for this purpose. Further, droplet detection system used for this study and its fundamentals are explained in detail together with the motivation of the project.

1.1 Microfluidics

Microfluidic technologies are generally the type of systems that can handle and manipulate fluids (gas or liquid) in micron to nano scales. Microfluidic technologies can provide solutions to miniaturize macroscopic reactions and equipment running in the wet lab into a micron/nano scale device. Currently, microfluidic systems are mostly utilized in chemical and biomedical/biological applications as miniaturized analytical technologies which are called a micro-total analysis system (μ-TAS) or lab-on-chip (LOC). Although both terms are being used interchangeably, μ-TAS is mostly used for a type of chips that can integrate all laboratory processes needed for a specific purpose on a single chip, whereas LOC chips can run several processes on the chip and they are a subcategory of μ-TAS [1]. Miniaturization brings several advantages over conventional laboratory systems including less reagent consumption, less expensive experiments, less risky experiments while working with hazardous material, less contamination, increased reaction speed, increased sensitivity, specificity and reproducibility of reactions.

Development of microfluidic technology roots back to the microelectronic industry. Using the same infrastructure microelectromechanical (MEMS) systems started to develop and as a fluidic branch of MEMS, microfluidics technology flourished. Silicon is the major material of the microelectronic industry, and due to its standard fabrication processes, it had been in use for early microfluidic devices. However, the fabrication of microstructures on silicon wafer is limited to several micrometers. In addition, silicon is relatively expensive and opaque material that limits the optical detection. To overcome limits of the silicone, Whiteside group introduced soft lithography technique which opened the doors for microfluidic technology to become a wide field of research [2–4]. Glass and polymer both are transparent and relatively much affordable than silicone. Polymer materials such as polydimethylsiloxane (PDMS), polymethylmethacrylate (PMMA), polycarbonate (PC), and polystyrene (PS) have been utilized for fabrication of microfluidic channels [2–8]. Among all polymeric materials, PDMS is widely used for research purposes due to its easy molding process, low cost, and optical transparency. Microfluidic devices fabricated using PDMS and glass extensively have been utilized in various applications, such as drug delivery and discovery [9, 10], to cellular studies [11–15], DNA analysis [16–23], immunoassays [24–27], material synthesis [28], and studying chemical reactions [29–31].

1.1.1 Physics of Microfluidics

Herein, physical fundamentals in microfluidics have been reviewed. One of the fundamental properties in microfluidics is the length scale. The length scale in microfluidics is in micrometers, transition region from macro scale to nano scale. In this length scale, continuity assumption holds true due to the much larger length scale than mean free path of molecule motion [1, 32]. Therefore, at any point of the flow, fluid properties (e.g. pressure, density, and velocity) remain constant. Most of the fundamental equations governing for the macroscale fluid flow are applicable for microfluidics as well. However, as length scale decreases, effect of the viscous forces increase and become more dominant in comparison to bulk fluid flow in which inertial effects are more dominant than viscous effects. Additionally, surface effects become more crucial and must be considered due to increased surface-to-volume ratio and main mass transport mechanism changes from convection to diffusion [1]. Following parts demonstrate basic principles governing the fluid flow in microfluidic systems.

1.1.1.1 Mass Conservation Principle

Assuming that there is a steady flow inside a tube (inlet and outlet flow are independent of the time), it can be stated that rate of the mass entering into a system is equal to the rate of the leaving mass. Principle of the mass conservation is expressed as equation (1.1) and named as 'Continuity equation',

$$A_1\rho_1 u_1 = A_2\rho_2 u_2 \tag{1.1}$$

where A_1 and A_2 are cross sectional area of the tube, ρ_1 and ρ_2 are fluid densities and u_1 and u_2 are the fluid velocity in cross sections of the tubing.

1.1.1.2 Energy Conservation Principle

Bernoulli's principle in fluid mechanics explains the fluid behavior in steady-state, inviscid flow and it can be derived from the principle of energy conservation. Bernoulli's principle states that, in a fluid flow, an increase in fluid velocity occurs simultaneously with a decrease in fluid pressure provided that the height of the fluid remains constant. Bernoulli's equation can be written as,

$$\frac{P}{\rho} + \frac{1}{2}v^2 + gh = constant \tag{1.2}$$

where, P is the fluid pressure at the specific point; ρ is the fluid density; v is the velocity of the fluid at the specific point; g is the gravitational acceleration; and h is the fluid height difference from a reference plane.

1.1.1.3 Poiseuille's Law

Poiseuille's law, also known as Hagen-Poiseuille law, applies for laminar viscous flow inside circular smooth channels and it can be derived from Navier-Stokes equations. According to this equation, a pressure difference between inlet and outlet of a channel is needed to establish fluid flow. Poiseuille's equation can be written as,

$$\Delta P = \frac{8\mu L Q}{\pi r^4} \tag{1.3}$$

where, ΔP is the pressure difference between inlet and outlet; μ is the fluid dynamic viscosity; L is the tubing length; Q is the flow rate; and r is the internal radius of tubing.

In general, most of the microfluidic channels are fabricated as either rectangular or semi-circular shapes due to fabrication simplicity in comparison with circular channels. Poiseuille's equation for rectangular channels where width w is much larger than the height, h, $(w \gg h)$, can be written as,

$$\Delta P = \frac{12\mu L Q}{w h^3} \tag{1.4}$$

and for semi-circular channels with radius of curvature of r, pressure drop will be in the form of,

$$\Delta P = \frac{64\mu L Q}{3 r^4} \tag{1.5}$$

Equations (1.3) to (1.5) are all written for the smooth channel case. In practice, there is always roughness factor, which is usually neglected, however roughness increases pressure drop inside channel and it has to be considered. Taking the friction factor (C_{fr}) and hydraulic diameter of the channel D_h into Poiseuille's equation, it can be written as [33–35],

$$\Delta P = C_{fr} \frac{\mu L Q}{2 A D_h^2} \tag{1.6}$$

where, C_{fr} is 64 for circular channels and 96 for rectangular channels; and A is the fluid flow cross sectional area.

1.1.1.4 Important Dimensionless Numbers in Microfluidics

Investigating fluid flow is a complex physical phenomenon. Dimensionless numbers are used to overcome this complexity by reducing number of variables in a fluidic system. Correlating various parameters helps to decrease number of the required experimental data. Further, dimensionless numbers are used in engineering and physical problems to understand similarity. Some of the important dimensionless numbers used in fluid mechanics and specifically important for microfluidics are presented as follows.

Reynolds Number (Re)

Reynolds number is ratio of inertial forces to viscous forces in fluids which determines fluid flow regime. Reynolds number is defined as,

$$Re = \frac{\rho v l}{\mu} \tag{1.7}$$

where ρ is the fluid density, v is the velocity of the fluid, μ is the fluid dynamic viscosity, and l is the characteristic length. Characteristic length in channels is equal to the channel diameter and for any non-circular duct it is calculated using hydraulic diameter. Threshold of the Re number between laminar and turbulent flows inside channels is 2300. Due to decreased length scale in microfluidics in comparison with bulk fluid flow, viscous forces become significantly effective than viscous forces that leads to having laminar flow in most of that microfluidic devices (Reynolds number less than 2300).

Bond Number (Bo)

Bond number is the ratio of capillary forces to gravitational forces. This number is important whenever surface tension is significant. It is defined as,

$$Bo = \frac{\rho g l^2}{\sigma} \tag{1.8}$$

where ρ is the fluid density; g is the gravitational acceleration; l is the characteristic length; and σ is the surface tension. Bond number is important specifically for droplets and bubbles moving inside another fluid. Low values of Bo number

($Bo < 1$) indicates that surface tension effects are significant and dominates the flow.

Weber number (We)

Weber number is the ratio of inertial forces to surface tension and it becomes important whenever there an interface between fluids which is the case for multiphase flows [36]. We is described as,

$$We = \frac{\rho v^2 l}{\sigma} \tag{1.9}$$

where ρ is the fluid density; v is the velocity of the fluid; l is the characteristic length (droplet diameter); and σ is the surface tension. In droplet microfluidics We number is crucial for droplet breakup. As channel dimensions decrease, We decreases and inertia becomes insignificant [37, 38].

Capillary number (Ca)

Capillary number is also important in microfluidic devices due to surface effects importance. Capillary number compares effect of viscous drag forces against surface tension forces. It is defined as,

$$Ca = \frac{\mu v}{\sigma} \tag{1.10}$$

where μ is the fluid viscosity; v is the velocity of the fluid; and σ is the surface tension. High surface-to-volume ratio of droplets inside microchannels makes surface tension an important parameter to be considered [39]. Droplets of different sizes can be generated by manipulation of Ca number [40].

1.2 Droplet-Based Microfluidics

Following the emergence of microfluidics field, several types of mixers, heaters and pumps were introduced for better manipulation of fluids in micro scale; however, they were not efficient in mixing due to Taylor dispersion [32]. For a while microchannels with long channel lengths were used to overcome the mixing problem.

However, it was not an efficient approach. Compared to single-phase microfluidics, droplet-based microfluidics has significantly increased reaction speed and mixing performance due to the high surface-to-volume ratio in microdroplets and the internal circulatory flow inside them. In droplet-based microfluidics, each individual droplet is considered as a microscale reactor that can be utilized for various applications, such as enzyme reaction [41], single-cell analysis [13, 42], biochemical detection [43], synthetic biology [44], and biotechnology [45]. In addition to increase reaction speed, droplet-based microfluidic systems have evolved to provide high-throughput, and consume less sample to reagent ratios. Figure 1.1 depicts a schematic droplet microfluidic system.

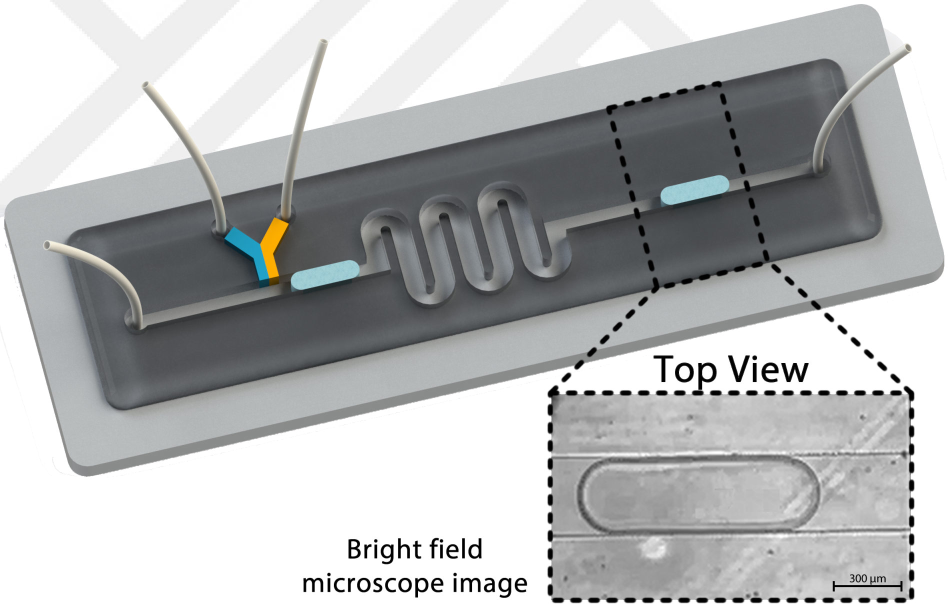

Figure 1.1: Droplet inside a microfluidic channel.

Conducting various biochemical synthesis and analysis inside microdroplets requires high sensitivity and droplet properties can greatly affect the synthesis and analysis results. Thus, there is a essential need for quantitative and qualitative monitoring ability inside droplet reaction chambers. Various detection techniques have been developed for droplet analysis [46, 47]; however, this thesis has focused on morphological detection techniques in droplets that are explained in the following section.

1.2.1 Droplet Detection Methods Inside Microchannels

So far, several droplet detection methods have been employed that can be categorized into three main principles of optical detection (light interaction with droplet), image-processing, and electrical detection. In the optical detection method, there is always a light source, e.g. LED, Laser, etc., and one or more photodiodes as a light sensor. As droplet moves through the sensor region it changes the refractive index of light also light intensity on the other side of the microchannel changes. Photodiode which acts as a light sensor constantly monitors incoming light and converts light intensity to electrical current. In this order, droplet passage can be monitored in an optical setup.

Most commonly used droplet detection system is the image-processing method due to its feasibility for most of the researchers worldwide. Image-processing studies has already developed softwares for droplet detection purposes and made them publicly available. Effectively, the only equipment needed for this method is the camera. Although image-processing has lots of advantages, it is computationally an expensive method that takes much more time for analysis than its counterparts.

The third method in use is electrical method that is either based on conductivity and permittivity changes of the matter. Impedance spectroscopy is one of the major electrical methods in which detection is done according to impedance change of medium, due to the difference in their dielectric properties. There are numerous flow cytometry studies in microfluidic chips which have utilized impedance spectroscopy as a label-free technique to investigate particle size, cell viability, and membrane composition [48, 49]. Due to the small scales of cells and particles, both resistive and capacitive components of impedance are used for analysis; however, monitoring systems for droplet analysis are based either on capacitive [50–53] or resistive sensors [54–56].

Figure 1.2 illustrates schematic setups used in current droplet detection systems inside microchannels. Further literature survey and details of them are presented in the following sections.

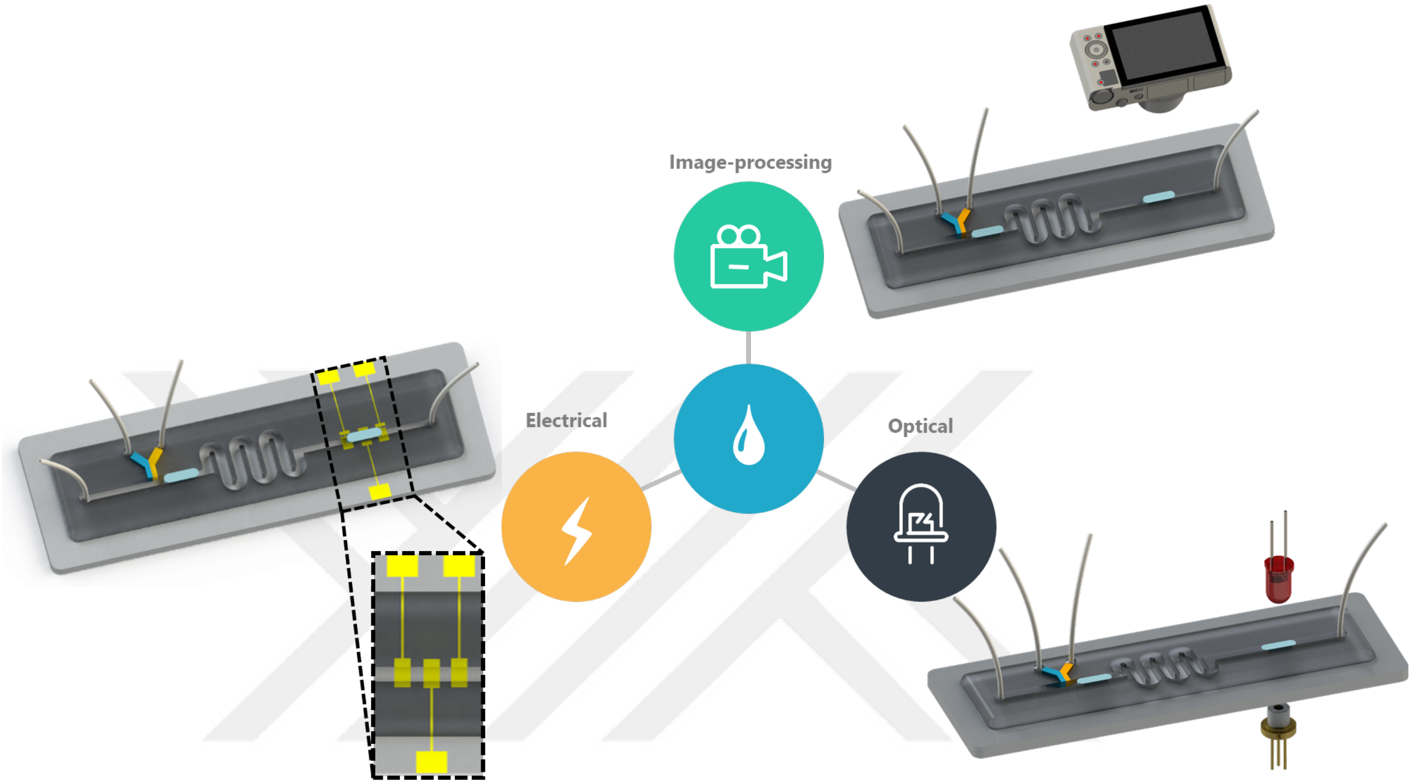

Figure 1.2: Droplet monitoring systems in microfluidic channels.

1.2.1.1 Optical Detection

Optical droplet detection was initially studied by Engl *et al.* to investigate droplet motion behavior at low capillaries. Using two He-Ne laser and photodiodes in a simple T-junction geometry with two branches they examined droplet motion behavior in various hydrodynamic resistances [57]. Nguyen *et al.* made a microfluidic chip with poly methylmethacrylate (PMMA) and they embedded a laser and photodiode inside the chip. In a syringe pump driven system (constant flow), assuming droplets as spherical, they wrote a force balance equation and managed to find an equation for droplet diameter [58]. Later De Saint Vincent *et al.* made a real-time droplet monitoring system using two laser beams to measure droplet size and velocity simultaneously [59]. Kunstmann-Olsen *et al.* made a setup for precise droplet splitting in a crossflow microfluidic channel. To achieve this goal, they prepared an optical setup consisting of a laser to detect and control droplet size ranging between 100 μm to 300 μm. Note that all droplets in this study are assumed as perfect circles. Hsieh *et al.* developed a setup for droplet size, velocity and composition sensing purposes in segmented flow using a laser with multiplying coupler integrated with two photodiodes on the other side for refractive index measurement [60]. Although recent optical systems are usually on-chip and do not require bench-top hardware, they suffer low reproducibility due to the challenging alignment of the light source with photodiodes. To overcome alignment issues, Bettella *et al.* benefitted lithium niobate ($LiNbO_3$) to bring self-alignment ability [61]. Eventually, Hassan *et al.* developed an optical setup by micromilling and embedding an LED and photodiodes inside a tiny gadget to make a point-of-care (POC) device. In their studies they have demonstrated droplet size, velocity and composition measurement with an application for colorimetric glucose sensing [62, 63].

1.2.1.2 Image-processing

Among different tools for the image-processing method, some studies used ImageJ software to measure the properties of a limited number of droplets [64–66]. ImageJ is an image-processing software written in Java with a publicly available source code, developed for general purposes which may require specific plugin development for specific needs. To overcome the limitation of software development, Basu developed an image-processing software based on MATLAB, extensively equipped for droplet studies called as droplet morphometry and velocimetry (DMV) that helps researchers to analyze various properties of droplets in large numbers [67]. Similarly, Chong *et al.* developed another image-processing tool named as automated droplet measurement (ADM), with the same functionality as DMV but with minimum inputs needed from the user side. Basically, ADM is an enhanced and automated version of DMV [68].

Recently, a real-time image-processing program has also been developed by Esmaeel *et al.* [69]. This program is developed under LabVIEW Vision development module. Therefore, it is required to have license of both LabVIEW and

Vision development module to operate this software. It has both online and offline analysis ability in analysis of circular shapes such as, circular droplets, RBC, particle inside droplet, and etc.

1.2.1.3 Electrical Detection

For electrical droplet detection, Niu *et al.* reported a capacitive detection method for counting droplets and droplet size, velocity and composition detection [70]. Elbuken *et al.* made non-contact planar microelectrodes to measure microfluidic droplet size and velocity using an application-specific integrated circuit (ASIC) [52]. Dong *et al.* utilized a multi connection interdigital electrode design to vary the size of the sensor to obtain a higher capacitance change for increasing droplet size [71]. Yakdi *et al.* investigated both plug-like and slug-like droplets to detect their size and velocity [72]. Fu *et al.* developed a capacitive droplet detection unit as part of a closed-loop control system to obtain a precise droplet size. They verified their electrical droplet detection results against an image-processing method [73]. Moiseeva *et al.* investigated both two-electrode and three-electrode detection mechanisms [74]. It was stated that a three-electrode differential measurement scheme eliminates the background drift. Additionally, since the size and velocity mutually affect the detection signal, these two parameters cannot be resolved using a two-electrode system.

To compare electrical and optical droplet detection methods, it can be stated that both are very similar regarding the signal that they process, however, electrical detection has a significant advantage in terms of fabrication and reproducibility. For the case of image processing, it is limited to the chip and droplet transparency which is not the case for electrical detection. In addition, computational power limits image-processing to the PC devices and it cannot be integrated on simple electronic boards that are being used for POC devices. Therefore, this study continued with the electrical droplet detection method and the following section gives a brief introduction of electrical detection principles.

1.3 Impedimetric Detection of Droplets

In this project impedimetric sensing approach has been employed to detect droplets inside microchannels. Literature survey of this method has presented in previous sections. Following parts are focused on fundamentals of impedance spectroscopy and measurement techniques.

1.3.1 Fundamentals of Impedance Spectroscopy

Impedance spectroscopy is a sensitive technique used for measuring the electrical properties by applying a small amplitude AC signal [75]. It has long been studied and used for investigation of dielectric properties in various applications concerning the interface and the bulk materials. Impedance spectroscopy has two main categories of Electrochemical Impedance Spectroscopy (EIS) and other materials [75, 76]. EIS is used to study materials with strong ionic conduction ability whereas the second category applies to dielectric materials which have dipolar rotation mechanism for electrical conductance such as single crystals, glasses, polymers and etc. EIS is a powerful technique for label-free and non-invasive sensing of systems with a complex electrical resistance that makes it applicable for biomedical applications. Also, EIS is utilized in fields that are dealing with fuel cells, rechargeable batteries, liquid electrolytes, corrosion, fused salts [76]. This section provides the fundamentals of impedance spectroscopy theory.

Electrical impedance is measured as a ratio of the applied AC potential to the current response of the material. Assume that a sinusoidal small amplitude ($\simeq 1V$) potential is applied to a system. System response will be an AC current signal with the same frequency while having a phase shift. The general form of the applied voltage is,

$$V(t) = V_o \sin(\omega t) \tag{1.11}$$

where $V(t)$ is the potential; V_o is the potential amplitude; and the ω is the angular frequency. In a linear system, the response would have a similar general form with a phase shift as following,

$$I(t) = I_o \sin(\omega t + \varphi) \tag{1.12}$$

where $I(t)$ is the current response; I_o is current amplitude; and φ is the phase shift. In such a system impedance would be expressed as,

$$Z(t) = \frac{V(t)}{I(t)} = \frac{V_o \sin(\omega t)}{I_o \sin(\omega t + \varphi)} = Z_o \frac{\sin(\omega t)}{\sin(\omega t + \varphi)} = \frac{1}{\Upsilon} \tag{1.13}$$

where $Z(t)$ is the impedance; Z_o is the impedance magnitude; ω is the angular frequency; φ is the phase shift; and Υ is the complex conductance or admittance. Impedance is dependent on both amplitude of the applied potential and the phase shift due to the current response of the system which makes impedance a complex value, depicted in Figure 1.3.

Using Euler's formula, applied potential, its current response, and impedance of the system can be re-written in the following form,

$$V(t) = V_o \exp(j\omega t) \tag{1.14}$$

$$I(t) = I_o \exp(j\omega t - \varphi) \tag{1.15}$$

$$Z(\omega) = \frac{V(t)}{I(t)} = \frac{V_o \exp(j\omega t)}{I_o \exp(j\omega t - \varphi)} = Z_o \exp(j\varphi) = Z_o(\cos\varphi + j\sin\varphi) \tag{1.16}$$

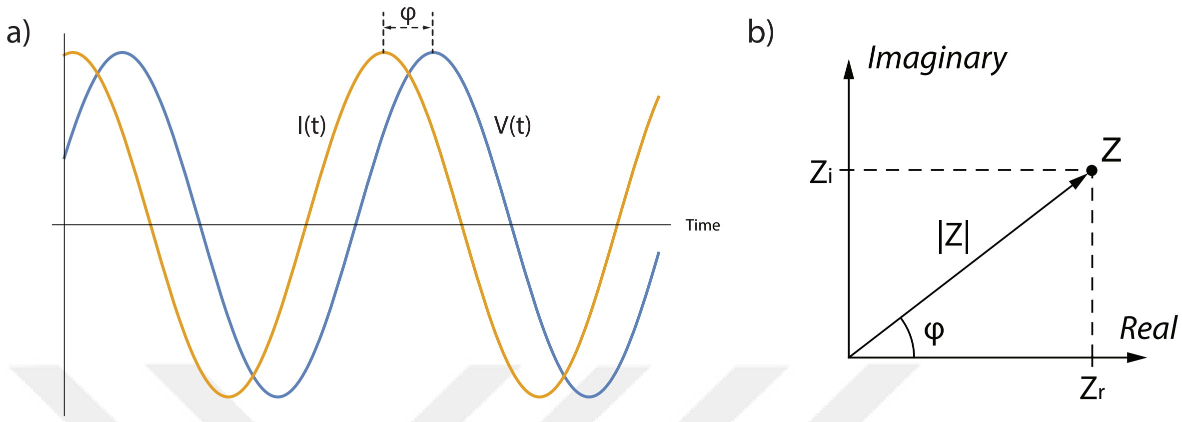

Figure 1.3: Impedance is a complex value that is defined as the quotient of the voltage ($V(t)$) and current response ($I(t)$) functions. a) Sinusoidal applied voltage ($V(t)$) and its current response ($I(t)$) in a linear system. b) Impedance (Z) can be expressed either by the real (Z_r) and the imaginary (Z_i) parts of the impedance or by the modulus $\mid Z \mid$ and the phase angle ϕ.

If $Z(\omega)$ is plotted with its real component on X-axis and imaginary component on Y-axis, a "Nyquist Plot" will be obtained, illustrated in Figure 1.4 (a). Impedance on the Nyquist plot is represented as a vector of length $\mid Z \mid$ and the angle between this vector and the X-axis is the phase angle (φ).

On the Nyquist plot lower frequencies are on the right side and as it increases from zero data points are plotted on the left. However, the frequency at which the data point is recorded is unknown in the Nyquist plot. Bode plot resolves the problem and plots impedance against frequency as depicted in Figure 1.4 (b).

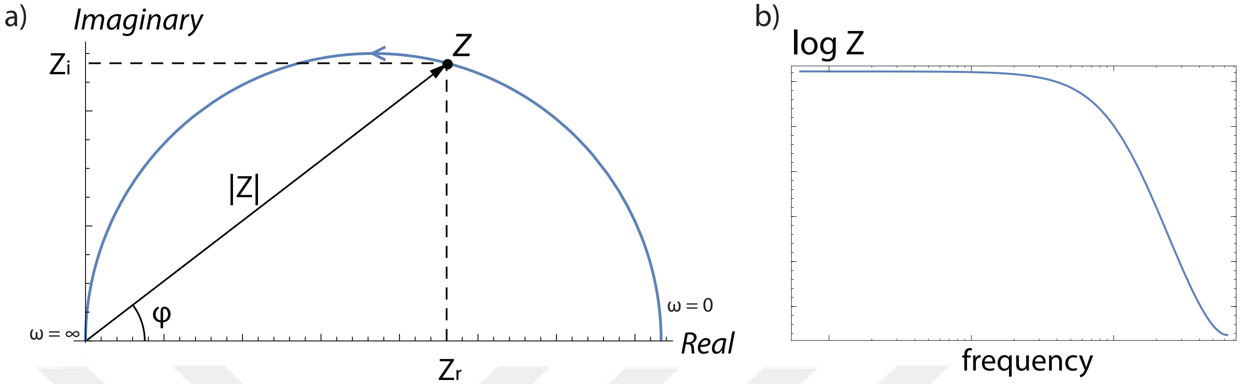

Figure 1.4: Representations of impedance $Z(\omega)$. a) Nyquist plot of the impedance (data points with lower frequency are on the right side and higher frequencies are on the left side). b) Bode plot of the impedance.

1.3.2 Measuring Impedance Using Lock-in Amplifier

To measure the impedance, which is a complex value, it is needed to measure at least two components. There are several approaches for impedance measurement including, bridge method, resonant method, I-V method, RF I-V method, network analysis method and auto-balancing bridge method [77]. Each of these methods is suitable for a specific frequency range. Impedance measurement technique that has been used in this thesis is based on a lock-in device following a transimpedance amplifier. Impedance change leads to current change, and the lock-in amplifier collects and amplifies the current. Transimpedance part converts the amplified current into voltage by multiplying current change into a fixed resistance, which is 1 kΩ for our case. Thus, the basics of lock-in amplifier working principle are presented as follows.

A lock-in amplifier is a sensitive AC voltmeter that can measure voltage amplitudes as small as few nanovolts buried in a noisy signal with small singal-to-noise ratio. Lock-in amplifier consists of five units: (i) signal amplifier, (ii) phase shifter, (iii) phase sensitive detector (PSD), (iv) low-pass filter, and (v) DC amplifier. Schematic of a basic lock-in amplifier circuit is shown in Figure 1.5. Input signal to be measured goes through an AC amplifier to be amplified.

On the other hand, a reference signal is generated, usually with unit voltage amplitude. Note that, $V_{reference}$ frequency should be in the frequency range of V_{signal} to lock-in on a specific desired frequency. The phase shifter makes a phase shift of 90° in dual-phase lock-in amplifiers to generate X and Y components. PSD or multiplier takes both V_{signal} and $V_{reference}$ and gives their multiplication. Using a low-pass filter (LPF) higher frequency component of the multiplied signal is filtered and only a DC term remains. To further increase the signal-to-noise ratio a DC amplifier is used.

If the input signal is in the form of,

$$V_{signal} = V_{sig} \sin\left(\omega_{sig} t + \varphi_{sig}\right) \tag{1.17}$$

where V_{signal} is the input signal; V_{sig} is the input signal amplitude; ω_{sig} is the input signal angular frequency; and φ_{sig} is the input signal phase shift.

The reference signal would be in the form of,

$$V_{reference} = V_{ref} \sin\left(\omega_{ref} t + \varphi_{ref}\right) \tag{1.18}$$

where $V_{reference}$ is the reference signal; V_{ref} is the reference signal amplitude; ω_{ref} is the reference signal angular frequency; and φ_{ref} is the reference signal phase shift.

Multiplied voltage signal in PSD will become as follows,

$$\begin{aligned} V_{PSD} &= V_{signal} V_{reference} \\ &= \tfrac{V_{sig} V_{ref}}{2} [\cos\left(\left(\omega_{sig} - \omega_{ref}\right) t + \varphi_{sig} - \varphi_{ref}\right) \\ &\quad - \cos\left(\left(\omega_{sig} + \omega_{ref}\right) t + \varphi_{sig} + \varphi_{ref}\right)] \end{aligned} \tag{1.19}$$

when ω_{ref} is locked on ω_{sig}, the time component of the first cosine term in equation (1.19) becomes zero,

$$V_{PSD} = \frac{V_{sig} V_{ref}}{2} \left[\cos\left(\varphi_{sig} - \varphi_{ref}\right) - \cos\left(\left(\omega_{sig} + \omega_{ref}\right) t + \varphi_{sig} + \varphi_{ref}\right)\right] \tag{1.20}$$

If the signal goes through a low-pass filter, signals with frequencies above the cut-off ratio of the low-pass filter will be filtered. In this way, the second cosine term of the equation (1.20) becomes zero, and the filtered signal becomes,

$$V_{LPF} = \frac{V_{sig} V_{ref}}{2} \cos\left(\varphi_{sig} + \varphi_{ref}\right) \tag{1.21}$$

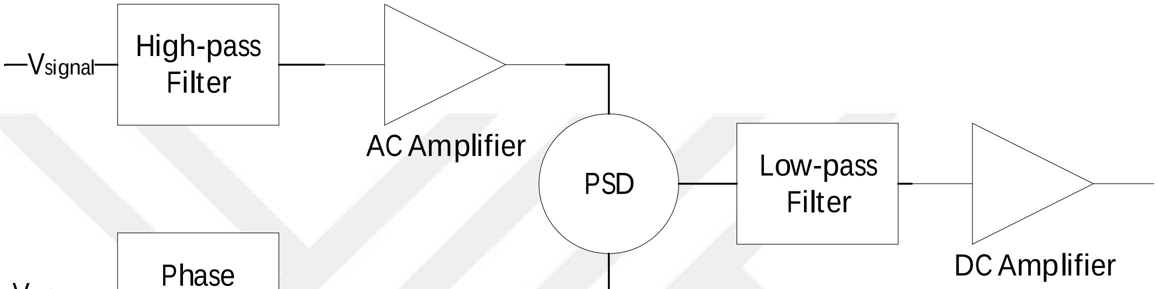

Figure 1.5: Schematic of lock-in amplifier circuit.

1.4 Motivation of the Work

Recent developments in droplet-based microfluidic systems have been discussed and their applications in biomedical and biochemical fields have been demonstrated. Increasing use of droplet microfluidics in different applications brought a significant need for droplet monitoring systems. Among different approaches that are already developed, impedimetric sensing has the ability for high-throughput, label-free analysis. Therefore, this thesis has focused on developing an impedimetric droplet sensing mechanism. Although several impedimetric droplet sensors have been developed, there is no real-time impedimetric droplet sensor. Further, among electrical or optical methods there are assumptions such as circle or rectangle droplets to simplify the detection procedure.

The current study presents a real-time impedimetric droplet sensor to monitor morphological properties of droplets. In contrast to all previous studies that have assumed droplets as circles or rectangles, the present system takes droplet cap length into equations and can monitor droplet length (L), cap length (CL), and velocity (V), simultaneously. Real-time droplet monitoring system gives us the ability to control the droplet generation system and test the effect of various parameters on droplets.

For instance, having a real-time droplet sensor, one can study the parameters affecting droplet morphological properties much more effectively. A major issue in all droplet-based system is the inherent assumption that all droplets are identical. Any variation in droplet volume reflects itself as an error for the analysis that is carried out. Hence, it is very important to investigate the droplet formation dynamics, preferably using a real-time analysis system. This thesis goes one step beyond that goal and also uses the know-how obtained for highly repeatable droplet generation for particle synthesis. As an example, polymeric particles of polyethylene glycol were synthesized using droplet microfluidics.

Chapter 2

Design of the Device

To design the microfluidic device, series of numerical simulations and optimizations have been conducted to have a better understanding of droplet sensor response and its performance. Afterwards, a design guide is presented for designing sensors suitable for different droplet length ranges. Discussions in this chapter are all dedicated to the numerical simulations and optimizations that are conducted by COMSOL Multiphysics v5.3 software.

2.1 Numerical Simualtions

A 3D model of the droplet and a multilayer structure of the microfluidic channel including gold electrodes and a passivation layer is prepared to investigate the response of the droplet sensor. Finite element simulations are performed using the electrostatics module of COMSOL. Governing equation of electrostatics in linear dielectrical materials, differential form of the Gauss's law, is exploited in this study as following,

$$\nabla.(\varepsilon_o \varepsilon_r \mathbf{E}) = \rho \tag{2.1}$$

where ε_o and ε_r are the free space and relative electric permittivity; $\mathbf{E}$ is the static electric field; and ρ is the polarization charge density.

The side-view schematic of the droplet model is shown in Figure 2.1. In this model, droplet leading and receding faces are considered as rounded with a constant radius of curvature. In the simulations, silicon oil (σ = 1 S/m, ε_{r} = 2.5) and water (σ = 5.5E-6 S/m, ε_{r} = 80) were used as the continuous phase and dispersed phase, respectively. There are three electrodes designated as left, middle and right. An electrical current study was performed by applying 1 V, 1 MHz potential to the middle electrode with respect to the side electrodes. A differential electrical measurement is performed by using the left electrode as the sensing electrode and the right one as the reference electrode. This gives a characteristic double peak signal for every droplet as shown in Figure 2.2. The motivation behind the simulations was to correlate the droplet position with respect to the electrodes and the corresponding real-time signal at any given point. Then, analyzing the real-time signal, we can determine the length and velocity of the droplet using simple algebraic equations.

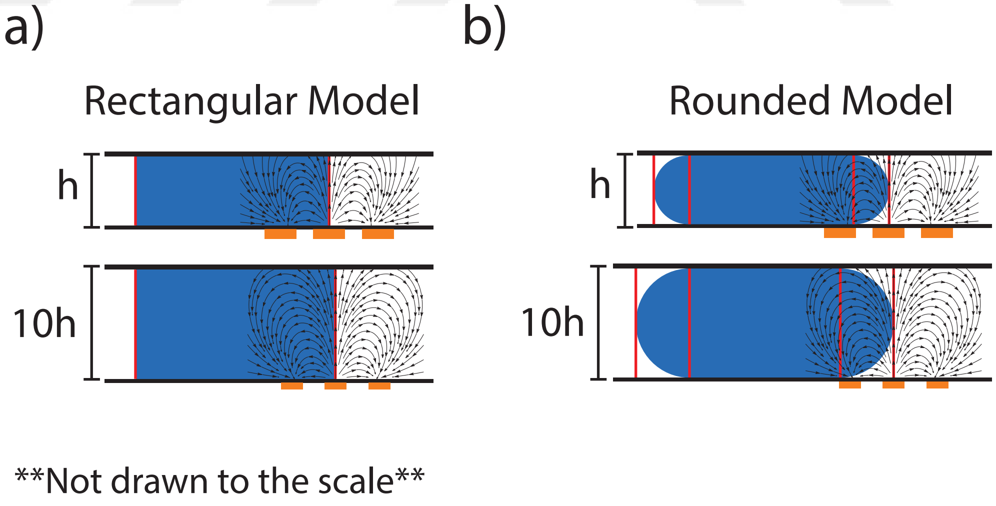

Figure 2.1: Schematic presentation of possible droplet simulation models. a) Rectangular droplet model. b) Rounded droplet model.

Microchannel height affects the impedance response of the droplet as illustrated in Figure 2.1. Electric field lines are given in Figure 2.1 to demonstrate the difference of the rectangular and rounded droplet models. In both models, droplet leading edge is positioned in the center of the middle electrode. Increasing microchannel height of the rectangular droplet model makes no difference in the electric fields covered by the droplet. However, it is evident that as channel height increases, rounded droplet covers less electric field lines, as illustrated in Figure 2.1 (b). Therefore, changing channel height changes the critical points of the characteristic signal (t_1 to t_8) corresponding to droplet location shown in Figure 2.2. Since the actual droplet shape is much similar to the rounded model than a cuboid one, the rounded droplet model is adapted for this study. Note that the microchannel height of 80 μm is used in all the following studies to match the experimental results.

Figure 2.2 gives the simulated signal when the droplet moves over the electrodes to the channel outlet at a constant velocity obtained by a parametric position sweep solution. To obtain this plot, the droplet was held stationary in the microchannel segment (length = 4000 μm, width = 300 μm, height = 80 μm) while the electrodes were moved in the opposite direction. In this way, we avoided the need for adaptive meshing. These results are obtained by a 3D geometry which matches the experimental conditions (Figure 2.2 channel inset), hence they represent the time domain signal obtained by the electrical detection signal. Assuming a constant droplet velocity, the x-axis can also be considered as the time scale. Therefore, the critical points on this position sweep plot are marked as t_1, t_2, ..., t_8, which are used in the calculations given at the end of this section.

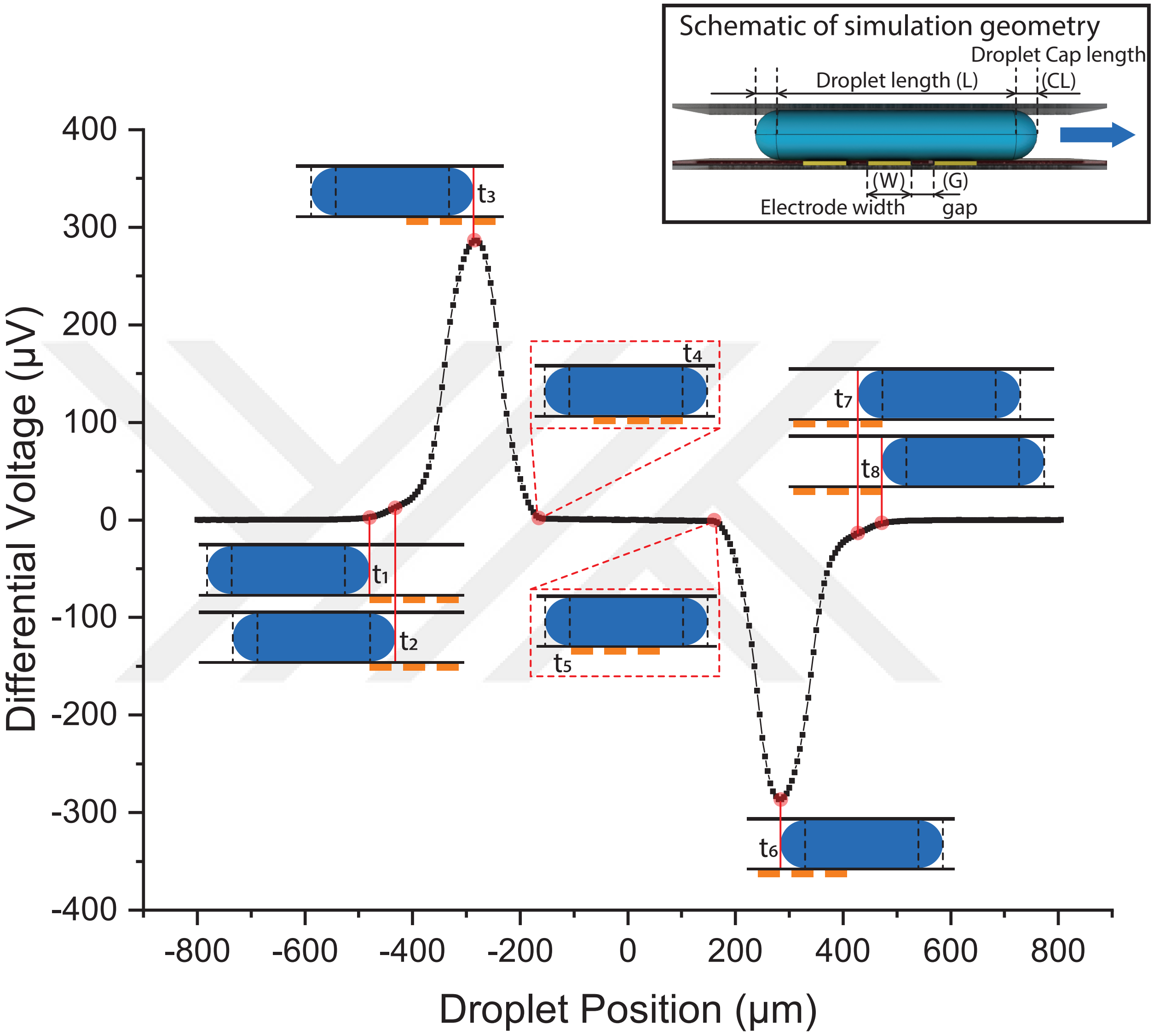

Figure 2.2: Differential voltage result as droplet position is swept for case 1, using L= 600 μm, CL = 40 μm, G = 25 μm and W= 75 μm. The current measured was read over a 1kΩ resistor (1 nA × 1 kΩ = 1 μV).

When a droplet enters into the sensing region, the voltage starts to increase at t_1 until t_3 at which the droplet completely covers the electric field between the left and middle electrode. On-going droplet motion toward the right electrode puts the droplet into the differential sensor region that in turn decreases the voltage until point t_4. The region between t_4 and t_5 is where the droplet entirely covers the symmetric electric field of the sensing and differential electrodes, hence no net voltage change is observed. The following region from t_6 to t_8 is the reciprocal of the region from t_1 to t_3.

The distance between the electrodes, gap (G), is another parameter to be considered. Herein, the simulation results are classified into two possible cases depending on the droplet cap length (CL) and gap (G) as depicted in Figure 2.3, $CL > G$ and $CL < G$. Although the characteristic signal shape in both cases is the same, there is a difference between case 1 and 2 stemming from different droplet positions corresponding to t_3 (maximum) and t_6 (minimum) points of the signal. The maximum of the signal occurs either when the droplet leading edge enters the right electrode region in case 1 or when it fully covers the middle electrode as in case 2. Due to the symmetric geometry of the simulation, the minimum has similar conditions as the maximum, illustrated in Figure 2.3. Although in case 1 the droplet is not fully covering the middle electrode, the peak voltage has a greater amplitude than case 2. Thus, increasing the gap is not desirable as this would decrease the peak voltage. Since case 1 gives a higher amplitude, resulting in a better signal-to-noise ratio, this study continued all the following analyses using case 1. For the channel height of 80 μm, we obtained a cap length of 40 μm. The electrode gap was set as 25 μm to be in case 1 domain.

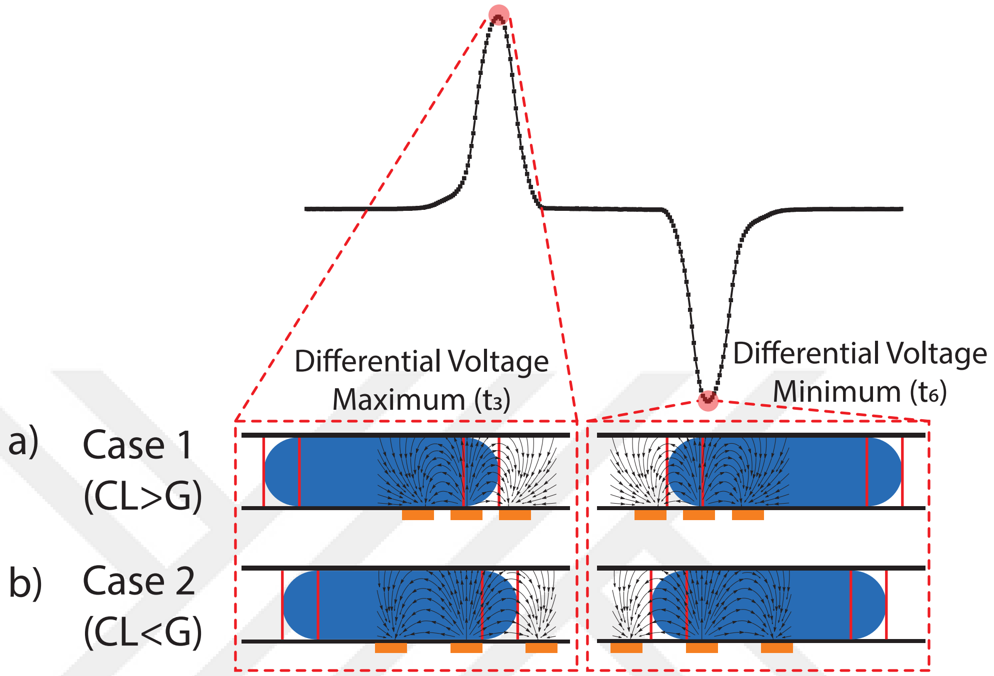

Figure 2.3: Schematic presentation of electrode gap (G) induced peak shift in possible droplet simulation models. a) Case 1. b) Case 2.

Eight points of interest are marked in Figure 2.2. Matching the droplet positions and the corresponding electrical signal level, three linear equations with three unknowns of L, CL and V can be written as follows:

$$\begin{aligned} V\,(t_7 - t_2) &= L + 3W + 2G \\ V\,(t_6 - t_3) &= L + 2CL - W - 2G \\ V\,(t_5 - t_4) &= L - 3W - 2G \end{aligned} \tag{2.2}$$

In this set of equations, t_4 and t_5 play a significant role in droplet measurement that is investigated by analyzing simulation results for changing droplet length as illustrated in Figure 2.4. As droplet length increases from $L = 100\ \mu m$ to $L = 900\ \mu m$, the peak voltage and the signal width remain constant whereas the duration from t_4 to t_5 increases. Another conclusion drawn from these results is that, $L = 100\ \mu m$ is too small for the chosen geometry since t_4 and t_5 points are indistinguishable in the electrical signal. Thus, there is a minimum droplet length limit for the above equations to be applicable.

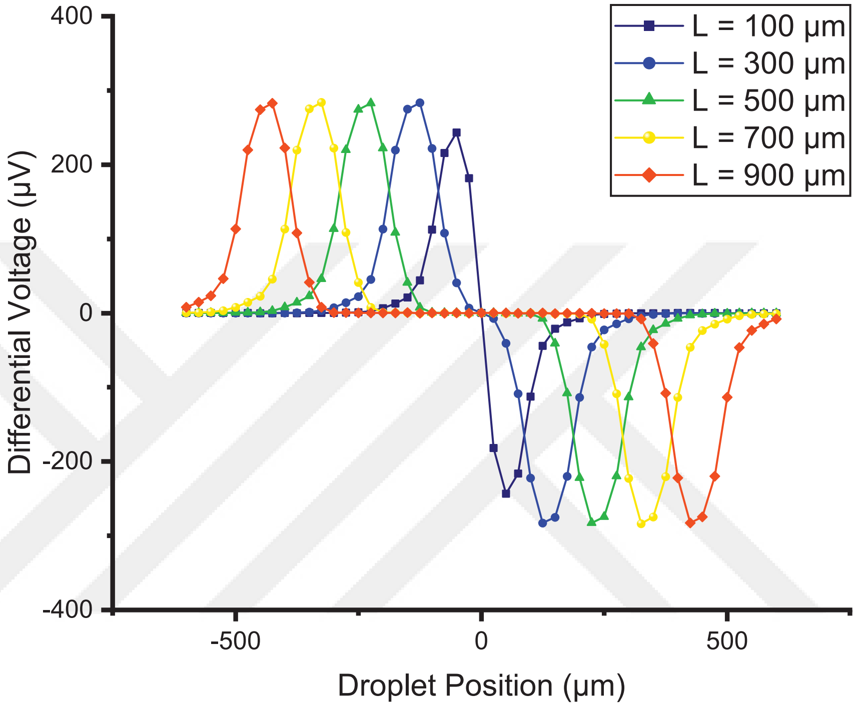

Figure 2.4: Droplet length sweep for case 1 (electrode configuration is $W = 75$ μm and $G = 25$ μm).

For the investigation of variation in cap length, droplet models with fixed droplet length of 600 μm with varying cap lengths were proposed. Droplet models varied from rectangular model to ellipse of radius 200 μm. The results are given in Figure 2.5.

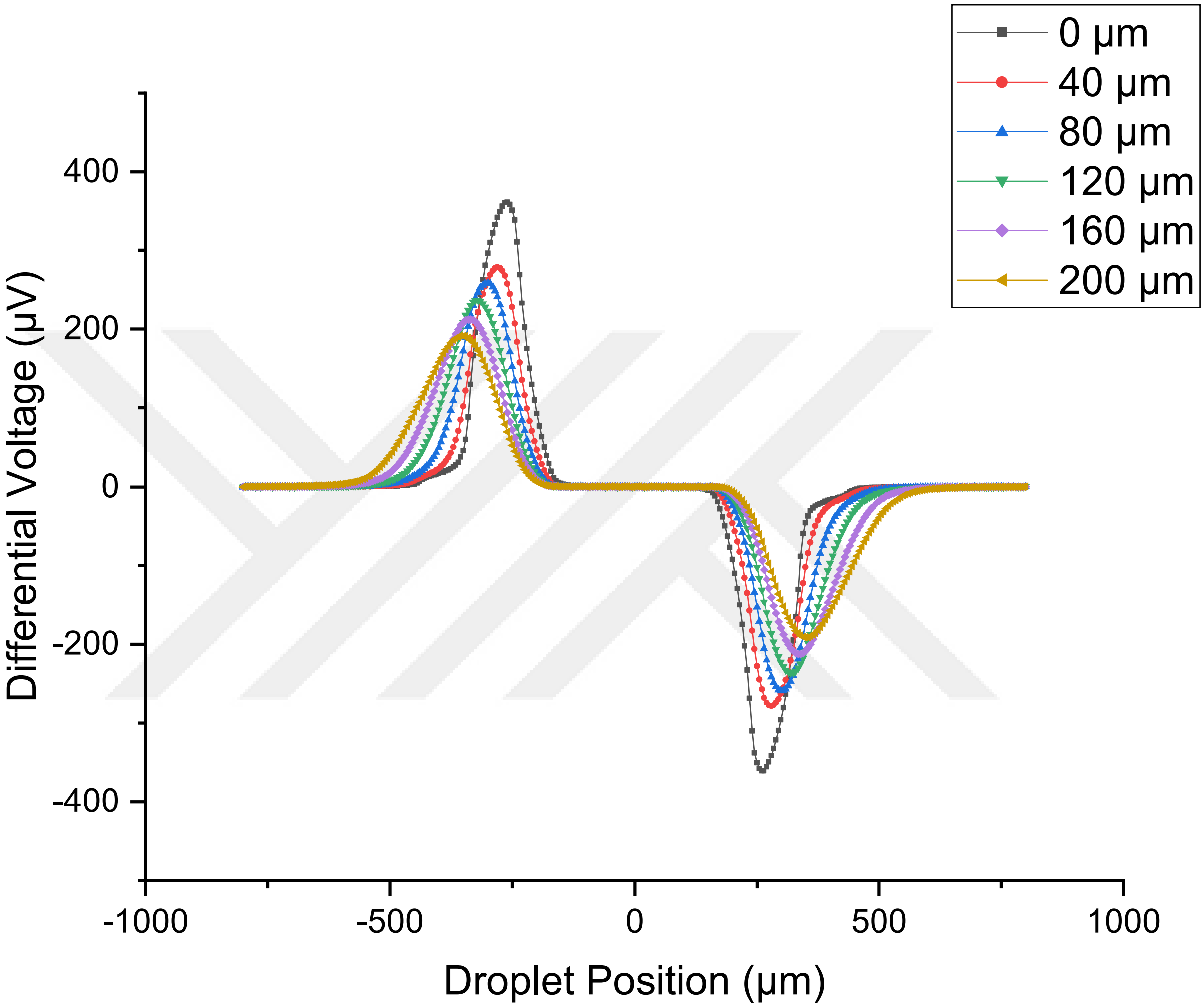

Figure 2.5: Droplet cap length sweep for case 1 (electrode configuration is $W = 75\ \mu m$ and $G = 25\ \mu m$).

If the droplet edges are close to circular, the peak position remains the same, and changing the cap length has a negligible effect on the signal shape. For large values of the cap length (much greater than the channel height) the peak decreases, and the slope increases at an earlier point. The reason for the peak decrease can be explained by the decrease of differential current for extremely long caps. As the conductivity over the channel increases at a slower rate while the droplet covers the electrodes, the signal shape becomes flattened. Likewise, while the left and center electrodes are fully covered, the right electrode has a large amount of water in the channel above it, so the differential voltage is much lower. In addition, such extreme cap lengths are indistinguishable from increasing the droplet length, hence the increase in the distance between the peak points.

2.2 Optimization

After the analysis of the characteristic signal, we studied electrode configuration (width and gap) numerically to achieve a high signal-to-noise ratio. The electrode width sweep in Figure 2.6 (a) shows that amplitude of the differential voltage increases uniformly with the increase of electrode width; however, if the length of the sensing region ($3W + 2G$) exceeds the droplet length (L), the maximum voltage decreases. The suggested electrode width region to obtain high signal-to-noise ratio is specified in Figure 2.6 (a). The electrode width should be maximized such that the electric field lines span a larger portion the channel depth as long as the sensing region fits into the droplet length.

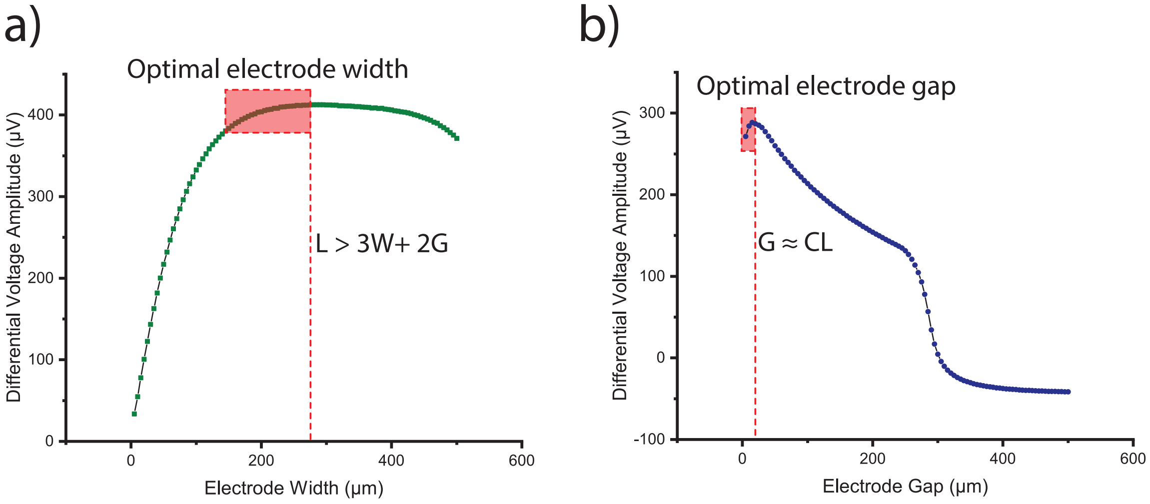

Figure 2.6: Electrode geometry optimization results. a) Electrode width sweep for a droplet geometry of $L = 600\ \mu m$, $CL = 40\ \mu m$. b) Electrode gap sweep for a droplet geometry of $L = 600\ \mu m$, $CL = 40\ \mu m$.

As demonstrated in Figure 2.6 (b), the maximum differential voltage uniformly decreases with increasing electrode gap as long as the gap is not smaller than the droplet cap length. Moreover, there is a sudden drop in differential voltage at $G > 250\ \mu m$ due to the electrode sensing region exceeding the droplet size, which is beyond the detection range of our sensor. As shown in Figure 2.6 (b), at $G = CL = 40\ \mu m$, there is a peak of differential voltage amplitude. Therefore, the optimal gap size is equal to the droplet cap length ($G \approx CL$), however, due to fluctuations in droplet generation, droplet cap length is inconsistent. As discussed earlier, since case 1 ($CL > G$) is always preferable for a better signal-to-noise ratio, an electrode gap distance less than the maximum should be set, as depicted in Figure 2.6 (b).

2.3 Design Guide

We also investigated the optimized electrode dimensions for droplets in the range of 300 μm to 1500 μm. The purpose of the simulation (provided in Figure A.1) is to provide electrode design guidelines to obtain a high differential voltage. The simulation sweeps the droplet length (L) from 300 μm to 1500 μm with steps of 100 μm, the electrode width (W) from 50 μm to 250 μm with steps of 5 μm and the electrode gap (G) from 20 μm to 40 μm with steps of 5 μm. The results show that it is required to decrease the gap and increase the width as long as the droplet can cover all three electrodes. The following boundary condition should be preserved,

$$L_{min} > 3W + 2G \tag{2.3}$$

where L_{min} is the minimum droplet length.

Once the above boundary condition is met, the width should be maximized and the gap must be minimized until approximately the droplet cap length ($G \approx CL$). In the region, when $W > 200\ \mu m$ and $L > 500\ \mu m$, the droplet size has almost no effect on the maximum differential voltage and increasing the electrode width yields an increase less than 5%. For the results shown in the supplementary document an electrode width of 150 μm is sufficient, since larger electrode width is contributing the voltage amplitude by less than 10%.

Chapter 3

Fabrication of Microfluidic Device

Among several microfabrication techniques for microchannels, soft lithography is widely adopted by researchers due to its ease of fabrication, which makes it suitable for prototyping of microfluidic chips. Based on standard microfabrication processes, fabrication of the device, consists of two parts of (i) mold fabrication for microchannels, and (ii) electrode fabrication. Following sections will provide in detail description of fabrication procedures utilized.

3.1 Fabrication of Microchannels

Soft lithography is a technique used to make micro structures on elastomeric materials which is developed by Whitesides lab [3, 78]. In softlithography, polymer takes the shape of the master mold. Standard soft lithography technique consists of two major procedures. Mold is designed and fabricated using photolithography technique, followed by the soft lithography in which, PDMS (polydimethylsiloxane) molding is done to fabricate the PDMS microchannels.

3.1.1 Photolithography

Photolithography is the most commonly used microfabrication technique for patterning of microstructures. Photolithography process transfers pattern of a photomask to a UV-sensitive polymeric film (photoresist) substrate using chemical etching. Photoresists are polymeric photoactive chemicals which are grouped in two main category of positive and negative. Positive photoresists become cross-linked during baking and UV light initiates depolymerization of the photoresist that leads to increased solubility of the UV-treated parts inside developer solution, however, negative photoresists become cross-linked in UV-treated regions, and do not dissolve inside developer solution. This method can be utilized for fabrication of microfluidic channels.

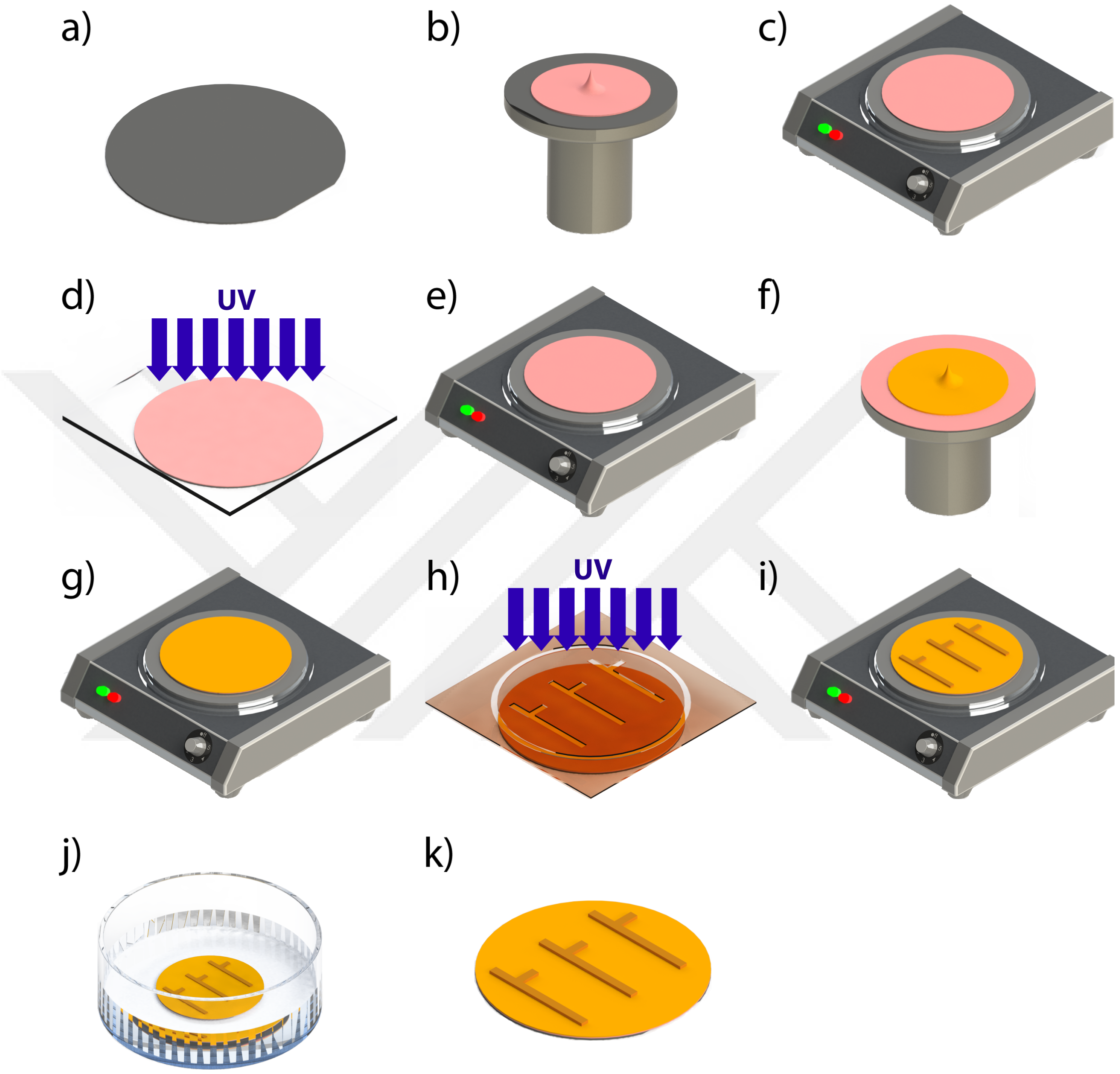

Figure 3.1: Schematic presentation of photolithography procedure applied for microchannel fabrication. a) pre-treatment of the silicon wafer. b) spin-coating of the SU-8 2005. c) soft-baking of the SU-8 2005. d) UV treatment of the SU-8 2005 with glass mask. e) post-baking of the SU-8 2005. f) spin-coating of the SU-8 2050. g) soft-baking of the SU-8 2050. h) UV-treatment of the SU-2050 with desired microchannel mask. i) post-baking of the SU-8 2050. j) removing unnecessary parts of the photoresist using SU-8 developer. k) rinsing and drying the mold.

Photolithography procedure utilized in this work is illustrated in Figure 3.1. A

4-inch silicon wafer is used as a master and two different SU-8 photoresists (MicroChem 2005, and 2050) were used as photoresists. Although SU-8 2050 is enough for standard photolithography, 2005 is used prior to, 2050, to prevent adhesion of PDMS to the silicon wafer. Initially, the silicon wafer is rinsed in acetone, isopropanol, and de-ionized (DI) water, respectively (Figure 3.1 (a)). Then, SU-8 2005 is spin coated on the silicon wafer (Figure 3.1 (b)), for 25 s with 500 rpm and 100 rpm/s acceleration, followed by a 50 s, 2500 rpm and 200 rpm/s acceleration, spinning to obtain 2 μm thickness. Ramped heating (65 °C for 2 min, 95 °C for 4 min and 65 °C for 1 min) is used to cross-link the photoresist to the wafer (Figure 3.1 (c)). Then, the wafer is cooled down until room temperature before proceeding with UV exposure to the photoresist. Using mask-aligner (EVG®620 Automated Mask Alignment System, Austria) 120 mJ/cm2 UV-light was exposed to the whole surface of the photoresist (Figure 3.1 (d)). For further cross-linking, wafer was put for another ramped heating process (65 °C for 1 min, 95 °C for 3 min and 65 °C for 1 min) after UV treatment (Figure 3.1 (e)). Afterward, SU-8 2050 was spin-coated at 500 rpm, with 20 rpm/s acceleration for 50 s followed by 1800 rpm, with 200 rpm/s acceleration for 40 s, to achieve 100 μm thickness (Figure 3.1 (f)). Then, the wafer was put on a hotplate for soft baking at 65 °C for 5 min, 95 °C for 10 min and 65 °C for 5 min (Figure 3.1 (g)). Next, the mask-aligner was used to UV treat the surface through the mask at 300 mJ/cm^2 (Figure 3.1 (h)). Then, it goes through another baking after UV exposure (Figure 3.1 (i)). Subsequently, the wafer was put into the developer solution of MicroChems SU-8 developer for 7 mins (Figure 3.1 (j)). Finally, the wafer is rinsed with water and blown by nitrogen to dry it (Figure 3.1 (k)).

3.1.2 Soft lithography using PDMS

In this case, PDMS is used to fabricate the microchannels utilizing soft lithography technique. PDMS was prepared by mixing the base polymer with a curing agent with 10:1 weight ratio. After proper mixing and degassing of the bubbles which were made during the mixing process, the mixture was poured onto the mold and it was cured for 4 hours at 100 °C. Later, the PDMS layer was peeled off and it was punched from inlets and outlets using biopsy punch.

Eventually, the PDMS microchannels were bonded with glass using a home made plasma asher. The oxygen plasma removes the hydrocarbon groups out of both PDMS and glass surfaces that activates silanol groups on the surface of the PDMS and OH groups on the glass substrate. Activated silanol and OH groups make covalent bonding possible between PDMS and glass slide.

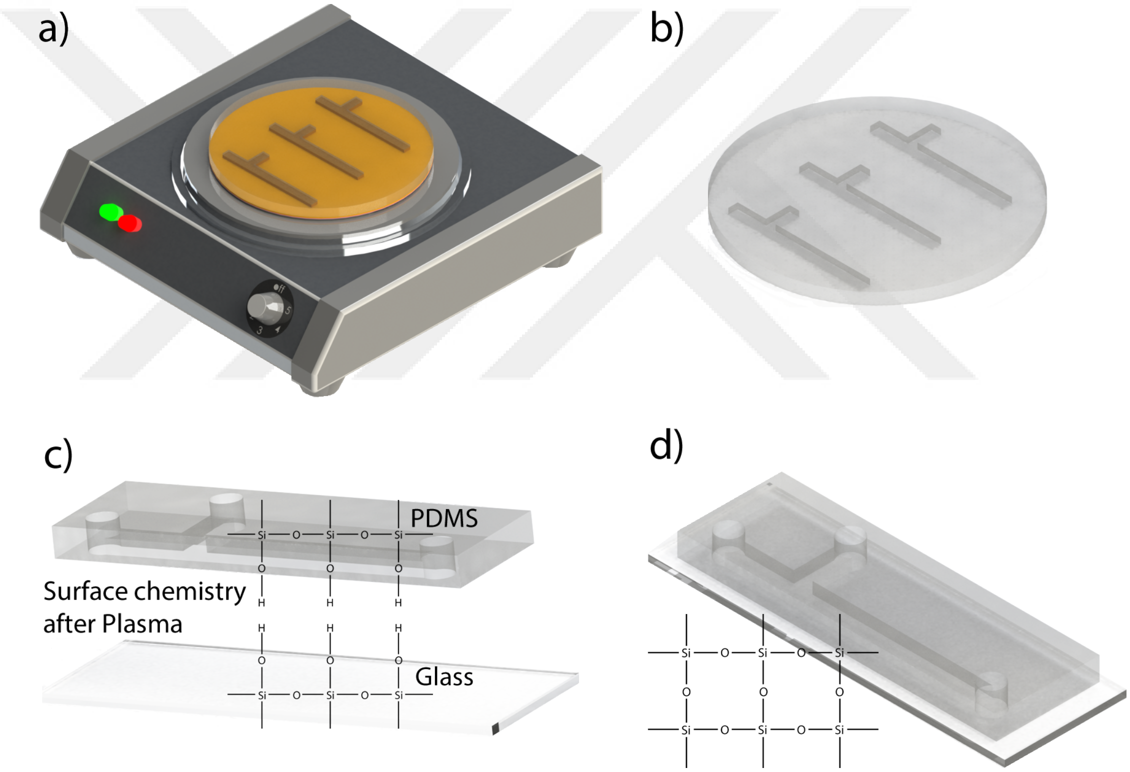

Figure 3.2: Soft lithography process of PDMS. a) PDMS mixture poured on the master mold and put on a hotplate for curing b) peeling-off the PDMS c) plasma bonding of PDMS with glass slide d) final microfluidic channels.

3.1.3 Tuning the Hydrophobicity

Usually microchannels become hydrophilic, specifically, right after plasma asher bonding. Hydrophilic channels change droplet formation dynamics and significantly affect droplet movement. To overcome this issue, a commercial product named CARPEX Rain Free was injected to microchannels, using a syringe, until filling the whole chip. After 1 minute, chip was put onto the hotplate at 80 °C for 10 minutes. If desired hydrophobicity could not be achieved in a single step, mentioned steps in applying Rain Free should be repeated.

3.2 Fabrication of Microelectrodes

To fabricate coplanar microelectrodes, it is needed to first make the desired electrode pattern using photolithography and then the metallic layer can be deposited on the surface of the developed photoresist. Finally, a passivation layer was deposited to avoid direct contact of the droplet with microelectrodes. Schematic representation of the microelectrode fabrication is shown in Figure 3.3.

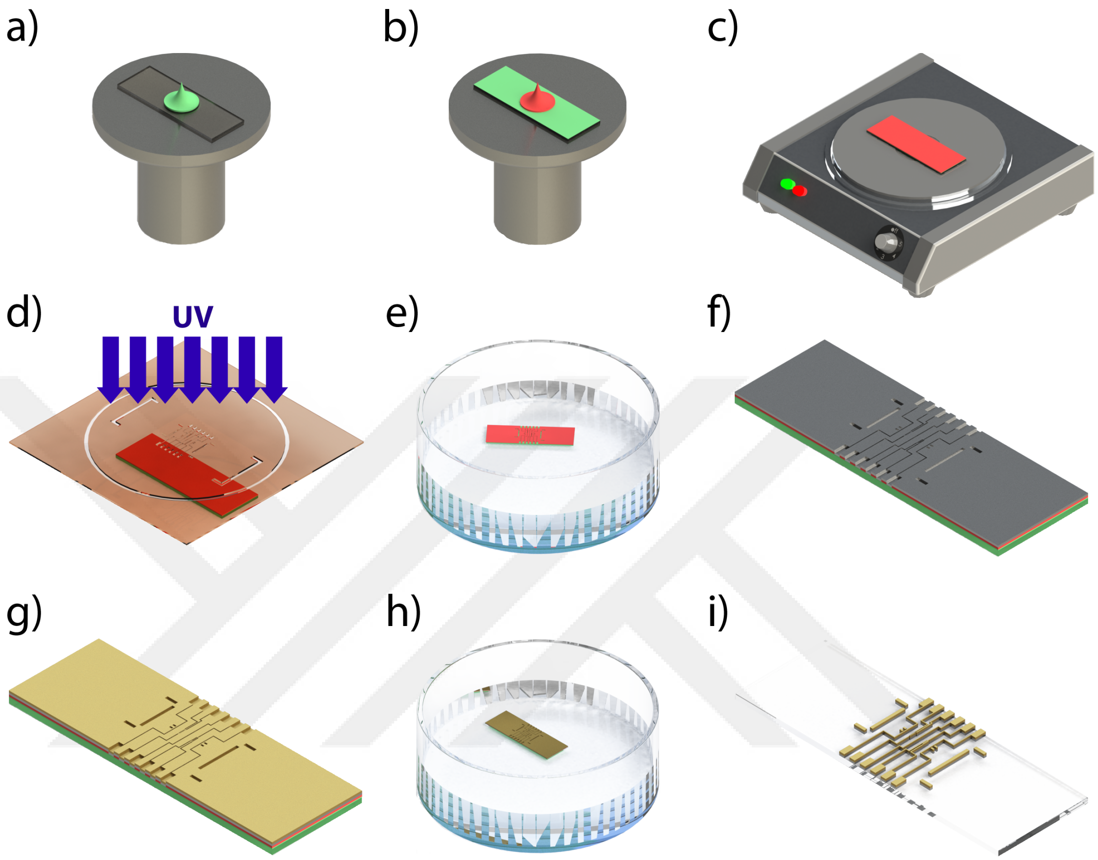

Figure 3.3: Schematic representation of microelectrode fabrication process. a) spin-coating of Hexamethyldisiloxane (HDMS). b) spin-coating of AZ5214E. c) soft-baking of the photoresist on a hotplate. d) UV-treatment of the substrate with a microelectrode patterned glass/chrome mask. e) rinsing the photoresist inside aqueous solution of AZ400K developer. f) deposition of a chrome layer. g) deposition of a gold layer. h) lift-off process inside acetone. i) rinsing the substrate with isopropanol and DI-water.

3.2.1 Photolithography

Coplanar electrodes were fabricated on a glass slide (26 mm × 75 mm) using photolithography and lift-off process. Prior to photolithography, the glass slide was rinsed with acetone, isopropanol and DI-water to remove contamination. Later, the glass slide was dried with nitrogen blow and was put on a 120 °C hotplate to ensure drying of any solvents. After that, Hexamethyldisiloxane (HMDS) was spin-coated at 5000 rpm for 40 s on the glass substrate to increase the adhesion of photoresist to the glass substrate. Subsequently, AZ5214E photoresist was spin-coated at 4000 rpm for 40 s. Later, the glass was put on a hotplate at 110 °C for 50 s to bake the photoresist. Then, electrodes were patterned using a glass/chrome mask with UV-light at 40 mJ intensity. The mask design process, needed for microfluidic channels and electrodes, were done in Tanner L-Edit (Mentor, USA) software by taking the results obtained from the finite element method (FEM) simulations into consideration. Finally, the photoresist was developed in an aqueous solution of AZ400K developer with 1:4 volume ratio of developer to water.

3.2.2 Metallic Layer Deposition

To fabricate gold electrodes on glass slides physical vapor deposition (PVD) method was utilized. PVD method consists of three steps: (1) vaporizing the source material, (2) transportation of vapor from source to the target, (3) condensing the vapor onto the substrate. The vapor can be transported by different methods (e.g., sputtering, thermal evaporation, etc.). Thermal evaporation is commonly used for deposition of low-melting-temperature metals (e.g., Au, Al, Ti, Cr). Herein, thermal evaporation is used for deposition of chrome and gold layers.

Using a thermal evaporator (Vaksis- MiDAS PVD 3T, Turkey), a 50 nm-thick Cr and a 100 nm-thick Au coatings are applied, respectively. Finally, a lift-off process was applied in acetone (Sigma-Aldrich, USA).

3.2.3 Passivation Layer Deposition

A passivation layer of SiO_2 was deposited onto the surface using E-Beam evaporator (Vaksis-MiDAS PVD 1eB, Turkey). The mixture was a 10:1 (w/w) ratio of

Sylgard 184 silicone elastomer and its curing agent (Dow Corning, USA). Then, after removal of the bubbles, the mixture was poured onto the mold and it was cured for 4 hours at 100 °C. Eventually, the glass was bonded with the PDMS microchannels using oxygen plasma.

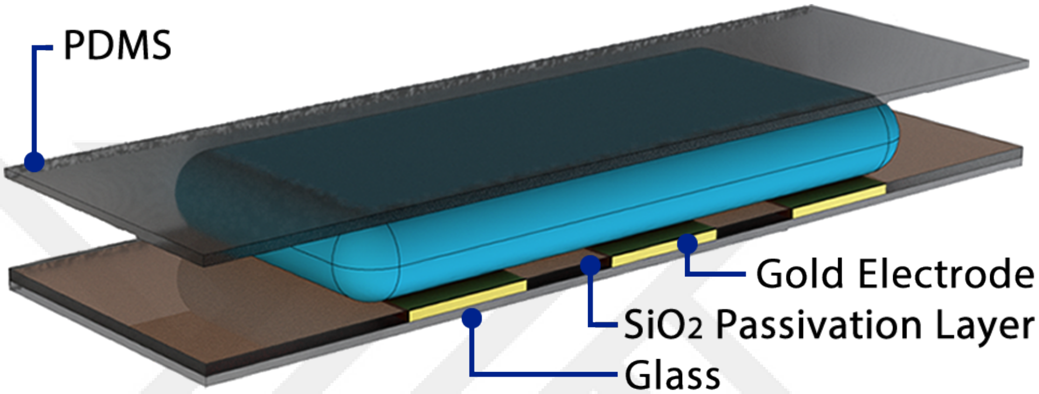

Figure 3.4: Schematic side-view of the microfluidic chip.

Prepared microfluidic device together with the setup is schematically illustrated in Figure 3.4. There is a simple T-junction geometry inside the microfluidic device for droplet generation. All the dimensions are selected according to the design guide. Droplet generation was performed using pressure-driven silicon oil (SF-50) and deionized water.

3.3 Fabrication of TWIST Valves

TWIST valves were first invented by Whitesides group as passive valves to control fluid flow inside PDMS microfluidic channels [79]. The concept of the valves is based on compression and expansion of the elastometic material (in this case PDMS) which has elastic behavior. TWIST valves include a bolt and a nut which are integrated inside PDMS. The nut inside the PDMS is fixed and the bolt moves by applying torque. Downward movement of the bolt in prependicular direction to the microfluidic channel compresses the channel that increases the channel resistance. Due to the elasticity of the PDMS, microchannels become to their original shape after opening (counterclockwise rotation) the bolt.

The first step in fabrication of a TWIST valve is to put the bolt and nut in a similar state as illustrated in Figure 3.5 (a). Next, the PDMS mixture was prepared as explained previously, and it was poured onto the bolt and nut until it exceeds the top face of the nut by 2-3 mm. After curing the PDMS on a hotplate, it was rotated and put on the PDMS mixture which is poured onto a master mold but it is still not cured. Finally, after the PDMS being cured, chip can be bonded and ready to use as shown in Figure 3.5 (b).

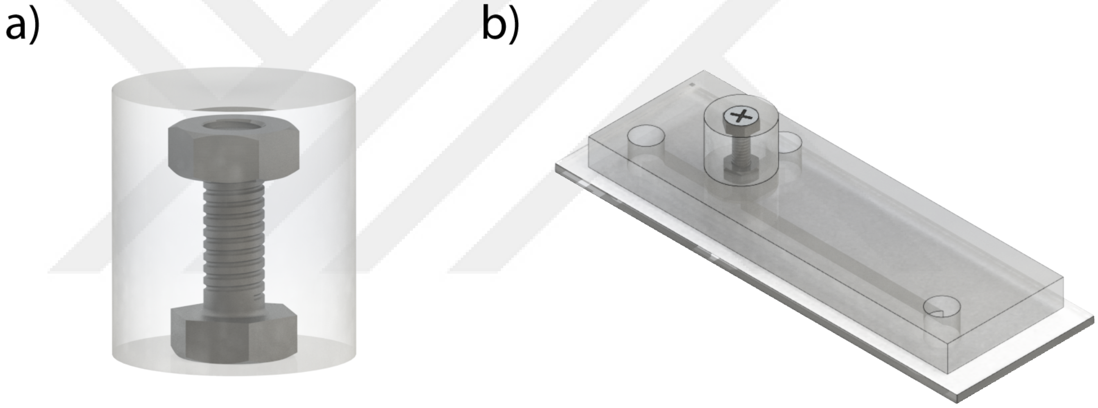

Figure 3.5: TWIST valve fabrication. a) fabrication of the valve. b) integration of the valve into PDMS microchannels.

Chapter 4

Impedimetric Droplet Measurement Software (iDM)

iDM software is developed using LabVIEW 2017 (National Instruments) platform to control and process differential electrical signals coming from a lock-in amplifier measurement system. For the case of this project, a DC - 50 MHz lock-in amplifier with 128-bit digital signal processing unit (HF2LI, Zurich Instruments) is used due to its availability in the lab. iDM can manipulate the lock-in amplifier device input parameters independent of the device control software (Zurich Instruments LabOne) made by the company; and also obtain the signals that are received by the lock-in device. Additionally, iDM processes the obtained signals and by detection of points of interest, and substitution of them into point of interest it can measure morphological properties of droplets such as length (L), cap length (CL), and velocity (V) in real-time. Also, iDM can be further developed for studying droplet electrical properties such as conductivity and dielectric constant. The algorithm is also optimized to be compatible with home desktop computers, and its logic is explained in the following part. iDM user-interface (UI) is designed user-friendly, with minimum input requirements from the user to provide an easy-to-use software for researchers in this field.

4.1 iDM Algorithm

iDM algorithm is developed for detection of eight points of interest (mentioned in Figure 2.2). The algorithm used for iDM consists of several blocks depicted as a flowchart in Figure 4.1 (a). 'Base block' is the main block of iDM which consists of seven blocks and it is used in point detection. Base block reads the incoming signal and detects t_1, t_2, ..., t_8. Afterwards, base block substitutes detected points into equation set (2.2), and calculates, shows, and saves L, CL, and V in real-time. To detect t_1, t_2, ..., t_8, differential voltage signal and its real-time derivate are used simultaneously. The reason behind using two signals simultaneously is to find points t_2, $\mathrm{t}_{\mathrm{m}1}$, $\mathrm{t}_{\mathrm{m}2}$ and t_7 that are easier to detect in derivative of the differential voltage signal (S'). Remaining points (red circles on S plot of the Figure 4.1) are detected using differential voltage signal (S).

4.1.1 iDM Algorithm in Detail

In this section a detailed algorithm of iDM is provided for further understanding of the program logic. Flowchart of each sub-program is depicted in Figure 4.2.

Explanation of iDM blocks:

- Base block: The 'Base block' controls the main flow of the program and it is explained in 'iDM algorithm' section.

- Gradient: 'Gradient' block is used by 'Point' blocks. This block constantly analyzes the incoming signal points in a moving window of five data points to detect the general trend of the data. Gradient block determines whether the signal is ascending, descending or at steady state. These states are named 'Positive', 'Negative' and 'Steady'.

- Point 1: This block determines t_1 using two conditions. The first condition to be met is that the data should be between the boundaries of lower limit (LL), and upper limit (UL) which are specified from the user side. The second condition

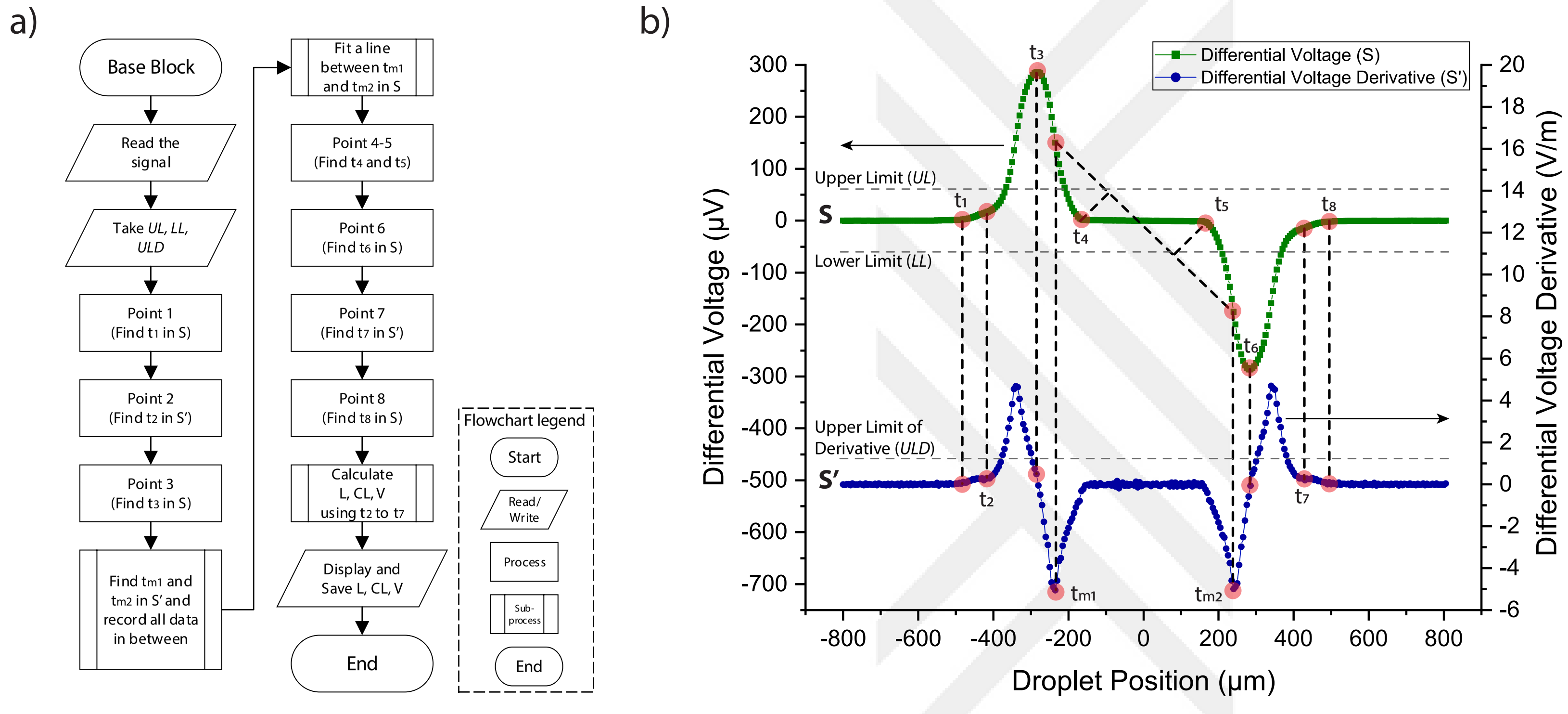

Figure 4.1: iDM algorithm for detection of t_1, t_2, $\ldots$, t_8 to determine L, CL and V. (a) Simplified flowchart of iDM algorithm. (b) Differential voltage signal (S) used for detection of t_1, t_3, t_4, t_5, t_6, t_8 and its derivative (S′) used for detection of t_2, $\mathrm{t}_{\mathrm{m}1}$, $\mathrm{t}_{\mathrm{m}2}$, t_7.

that has to be met is transition of state from steady state to positive state, which is determined through gradient block. If the first condition is satisfied, then the first data point after which the second condition is true is determined as t_1.

- Point 2: Detection of point t_2 using real-time differential voltage signal, depicted in Figure 4.1 (b), is complicated. Taking a derivative of the differential voltage helps to exactly identify t_2. The point t_1, is where the signal starts to increase from the noise region, however, at t_2, the only distinction is about slope change. Therefore, we have to analyze and find the point in which differential voltage signal (S') increases from the steady state to the positive state. The algorithm used for this point is similar to 'Point 1', however, S' is utilized instead. As depicted in Figure 4.2, t_2 is defined as the point where, S' should be less than the upper limit of derivative (ULD) and also state is changed from steady to positive on the signal derivative (S') plot. It should be noted that, the differential voltage derivative signal (S') given in terms of V/m corresponds to time derivative due to equivalence between droplet position sweep in simulations and actual droplet motion in time.

- Point 3: t_3 is the maximum point of the signal as illustrated in Figure 3 (b). Point 3 block is called after t_1 and t_2 were determined. Using the gradient block, point 3 looks for t_3 where the positive state turns into negative. There are two conditions defined to find this point. First, is the signal (S) should be more than UL, which guarantees that the point is not in the steady state. The second is to look for signal derivative (S') equivalence to zero, which indicates the point where slope is zero.

- Point 4 and Point 5: To find these two points, the program looks for the minimum points of the signal derivative (S'). The minimum points are named t_{m1} and t_{m2}, and their corresponding points on the signal plot are depicted in Figure 3 (b). Subsequently, a line was fitted on the signal (S) plot between the two points corresponding to t_{m1} and t_{m2}. Then, the two points of the signal (S) with maximum distances on either side to this line are calculated and identified as t_4 and t_5, respectively.

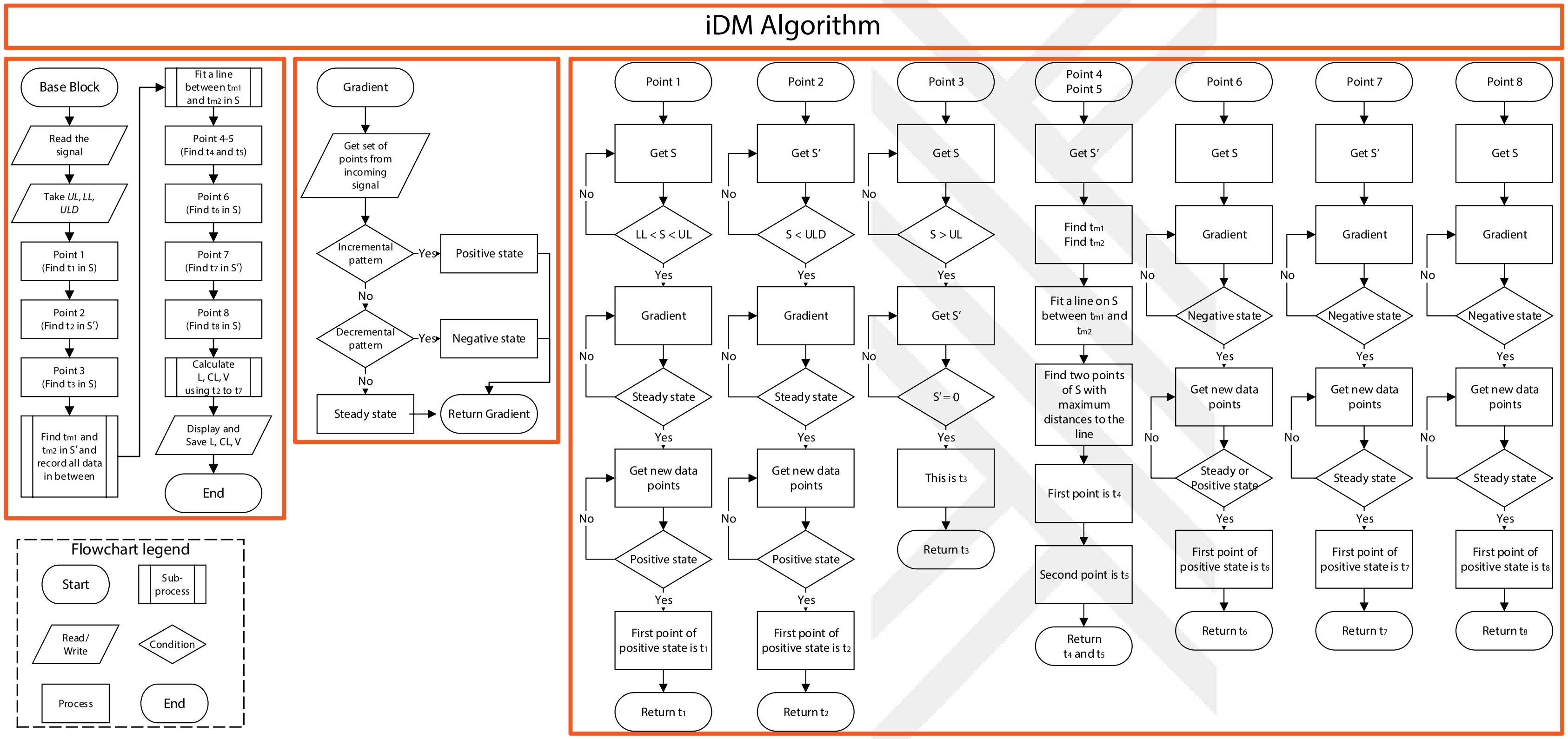

Figure 4.2: Complete flowchart of the iDM algorithm.

- Point 6: t_6 is the minimum point of the signal. Using the gradient block, point 6 looks for t_6 where the negative state turns into positive.

- Point 7: t_7 is defined as the state being changed from negative to steady on the signal derivative (S') plot and calculated using the Gradient block.

- Point 8: t_8 is defined as the state being changed from positive to steady on the signal (S) plot and calculated using the Gradient block.

Complete block-diagram of the iDM is presented in Figure C.1.

4.2 iDM Inputs and Outputs

iDM consists of two main sections named ‘Configuration’, and ‘Results’, illustrated in Figure 4.3. Figure 4.3 (a) depicts ‘Configuration’ part interface. To start obtaining real-time signal of the lock-in device I/O button on the top left corner of the program should be clicked. It may take couple of seconds for the device to set the default settings and get a stable signal. After initial start, ’Settings’ section allows the user to manipulate *Lock-in Amplifier* settings, set *Detection Thresholds*, and enter designed *Electrode Geometry.* In *Lock-in Amplifier* tab, demodulation frequency, demodulator data transfer rate (sampling rate), and excitation voltage can be manipulated and their default value are set to 1 MHz, 224.9 sample/sec, and 1 Volt. *Detection Thresholds* tab allows user to set three limits, Upper Limit (UL), Lower Limit (LL), and Upper Limit of Derivative (ULD), which are explained in the ’iDM Algorithm’ section. It is recommended to use 10-15% above and below the baseline signal (S) level as UL and LL, respectively. Similarly, the recommended ULD value is 10-15% above S' baseline signal. These limits can be determined by the user after visualizing the real-time droplet signal for the first few droplets shown in the ‘Configuration’ tab. Finally, after entering the microelectrode configuration (W and G) in *Electrode Geometry* tab, iDM is ready for signal processing.

a)

b)

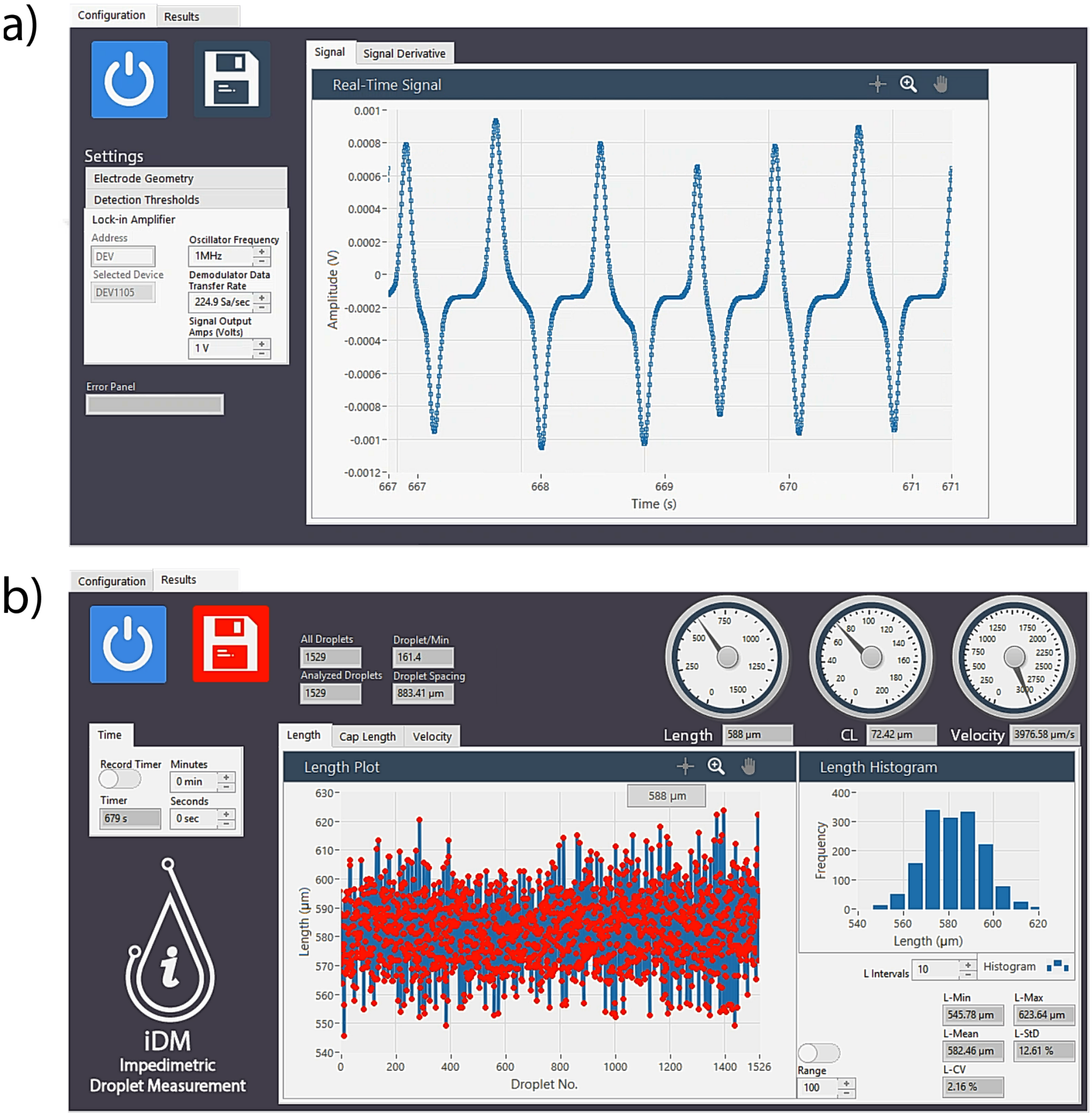

Address: DEV
Selected Device: DEV1105
Oscillator Frequency: 1MHz
Demodulator Data Transfer Rate: 224.9 Sa/sec
Signal Output Amps (Volts): 1 V

All Droplets: 1529
Droplet/Min: 161.4
Analyzed Droplets: 1529
Droplet Spacing: 883.41 µm
Length: 588 µm
CL: 72.42 µm
Velocity: 3976.58 µm/s
Record Timer
Minutes: 0 min
Timer: 679 s
Seconds: 0 sec
588 µm
L Intervals: 10
L-Min: 545.78 µm
L-Max: 623.64 µm
L-Mean: 582.46 µm
L-StD: 12.61 %
L-CV: 2.16 %
Range: 100

Figure 4.3: Screen-shot of iDM user-interface. (a) 'Configuration' tab interface. (b) 'Results' tab interface.

The second part of iDM called as ‘Results’ displays the three physical parameters of the droplets (length, cap length, and velocity) as output. The user can simultaneously monitor these parameters for the last detected droplets, as depicted in Figure 4.3 (b). Furthermore, the user can monitor the histogram, minimum, maximum, mean, standard deviation, and coefficient of variation of all these parameters in real-time. There is also *Time* tab to control and monitor data recording time. The number of total droplets detected by the electrodes and the ones that are successfully analyzed by iDM are given in the upper left section. As seen in the iDM screen capture image shown in Figure 4.3 (b), the algorithm was able to detect the 8 critical points and analyze all 1529 droplets. The average droplet generation frequency and droplet spacing is also shown.

Chapter 5

Impedimetric Droplet Measurement Setup

This chapter explains the microfluidic setup, designed for the impedimetric droplet detection system. The second part of this chapter focuses on method comparison methodology that is utilized to validate iDM results.

5.1 Experimental Setup

The setup used for impedimetric droplet detection inside the microfluidic chip is schematically illustrated in Figure 5.1. There are several approaches in microfluidic droplet generation [80, 81]. Herein, microfluidic chip design for droplet generation is based on cross-flow mechanism. Droplets were generated in squeezing regime, using a simple T-junction geometry (channel width = 300 μm, height = 80 μm).

Using a compressor and pressure source controller (Elveflow OB1) pressure is applied to glass vials, which are containing silicon oil (50 cST, Sigma-Aldrich) and deionized water. Glass vials were connected to the pressure source controller using needles (Metcal), Luer locks (Cole-Parmer) and Tygon tubings (Cole-Parmer). Using pressure source controller software (ESI v 3.02.05) air pressure for continuous phase (silicon oil) and dispersed phase was set. Since the continuous phase should be the dominant flow to generate water droplets inside silicon oil, it is required to have less hydrodynamic resistance in the oil channel than water channel. Therefore, either in addition to increasing water channel length to increase hydrodynamic resistance, applied pressure to the oil vial was more than water.

An inverted fluorescence microscope (Omano OMFL600) together with a high-speed camera (Phantom, Vision Research) was used to observe droplets inside microfluidic chip while experiments were running.

The microfluidic chip was equipped with coplanar electrodes for impedance measurements. Considering simulation results and having a wider range of droplet sensing, electrode gap of 60 μm and electrode width of 100 μm were preferred. A lock-in amplifier (Zurich instruments, HF2LI) were connected to the electrodes, as shown in Figure 5.1, through BNC cables and connectors. On the other side, lock-in device was connected to a PC using USB cable. Lock-in amplifier device can be controlled by both iDM and Zurich Instruments LabOne software.

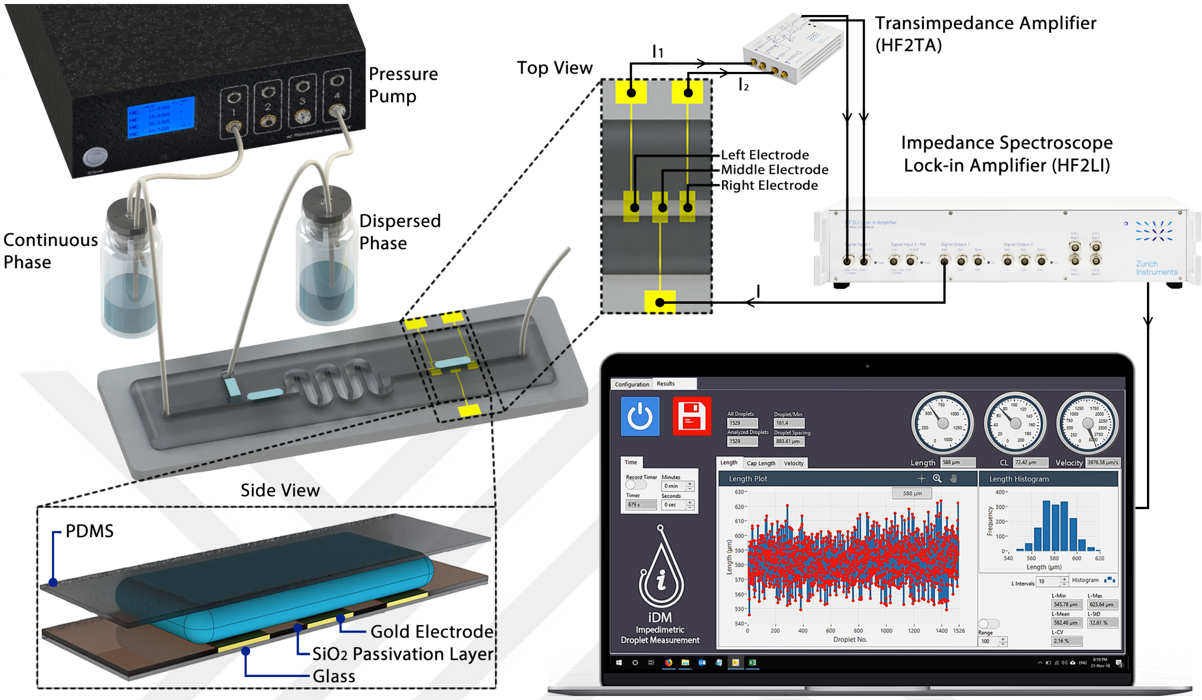

Figure 5.1: Schematic of impedimetric droplet measurement (iDM) setup consisting of a PDMS microfluidic chip equipped with three electrodes. Coplanar electrodes are coated with a passivation layer to prevent electrode deterioration with direct contact of electrodes and droplets. AC signal is applied through the middle electrode. A transimpedance amplifier is used to obtain the voltage signal, which is fed to the lock-in amplifier.

5.2 Verification of iDM

This part includes a brief summary of dominant microfluidic droplet analysis softwares and method comparison analysis between DMV droplet image-processing software, and iDM.

5.2.1 Methods Currently in Use

Currently, microfluidic droplet analysis is dominated with image-processing softwares due to their inexpensive and feasible requirements. Mainstream droplet analysis softwares are DMV [67] and ADM [68]. First image-processing tool that was introduced to droplet analysis field in 2013, is DMV. DMV allows the user to manually tune various parameters to control image-processing results. After image-processing, DMV offers a wide range of detailed analysis plots. Later, a new software (ADM) was introduced as a fully automatic alternative of DMV. ADM sets all image-processing parameters automatically that significantly decreases user training requirments. Further, the optimized algorithm of ADM has considerably increased processing speed, compared to DMV. This study used both DMV and ADM to compare their results with iDM. Obtained results in ADM and DMV were similar, therefore, for further analysis, DMV is employed due to its dominance in the field.

5.2.2 Method Comparison: iDM vs DMV

Method comparison methodology is employed to compare different methods, whenever none of the methods is reference method. It is important to spot the difference between method comparison and calibration in which one of the methods is accepted as a reference method (golden standard). In calibration analysis, a scatter plot with linear regression is used to compare two methods. Although, calibration method is often confused with method comparison, it is not enough for comparing two methods [82]. Method comparison consists of two main parts: (i) evaluation of similarity and (ii) evaluation of agreement [83].

Evaluation of similarity is required to understand and compare different characteristics including biases, precisions, and sensitives of methods [83]. When two methods have a poor agreement, the evaluation of similarity is helpful in understanding whether the poor agreement is due to the superior characteristics of one of the methods. Also, in some cases, methods can have poor agreement while having a similar characteristic that means having a good similarity cannot guarantee a good agreement. Therefore, the evaluation of similarity is not enough to evaluate the agreement of the methods.

Evaluation of agreement is fundamental to understand if the methods have sufficient agreement and whether they can be used interchangeably or not. Generally used method comparison approach for clinical applications was first proposed by Bland and Altman [82, 84, 85]. Due to useful information of Bland-Altman plot, this method was soon adopted in different studies than medical purposes [86–88]. Bland-Altman analysis provides a comprehensive comparison for the evaluation of data at specific ranges by relating the differences against the average of measurements (in each obtained data point). Using the Bland-Altman method, we can determine the limits of agreement and conclude the interchangeability of the methods.

Droplet size ($L+2CL$) is the most important property to be monitored. Having a reliable real-time system for droplet size analysis considerably improves droplet-based microfluidic studies. Therefore in the method comparison part, all the comparison are made using droplet size. Suggested least sample size, reported by Clinical & Laboratory Standards Institute, for clinical standards is 40 and for manufacturers is 100 [89], however, this study used over 1800 droplets for comparing iDM and DMV, depicted in Figure 5.2.

Evaluation of similarity is checked by fixed bias, proportional bias, precision, and sensitivity calculation. Fixed bias (β_0) and proportional bias (β_1) between the two methods are intercept (324.414) and slope (0.483) of Figure 5.2 (a), respectively.

For precision comparison of two methods, the precision ratio is used, defined as,

$$\lambda = \frac{precision\ of\ method\ 2}{precision\ of\ method\ 1} = \frac{1/\sigma_{e2}^2}{1/\sigma_{e1}^2} = \frac{\sigma_{e1}^2}{\sigma_{e2}^2} \tag{5.1}$$

where σ_{e1}^2 and σ_{e2}^2 are the variances of method 1 and 2, respectively. For the data given in Figure 5.2 (a) variances of iDM and DMV are calculated as 91.71

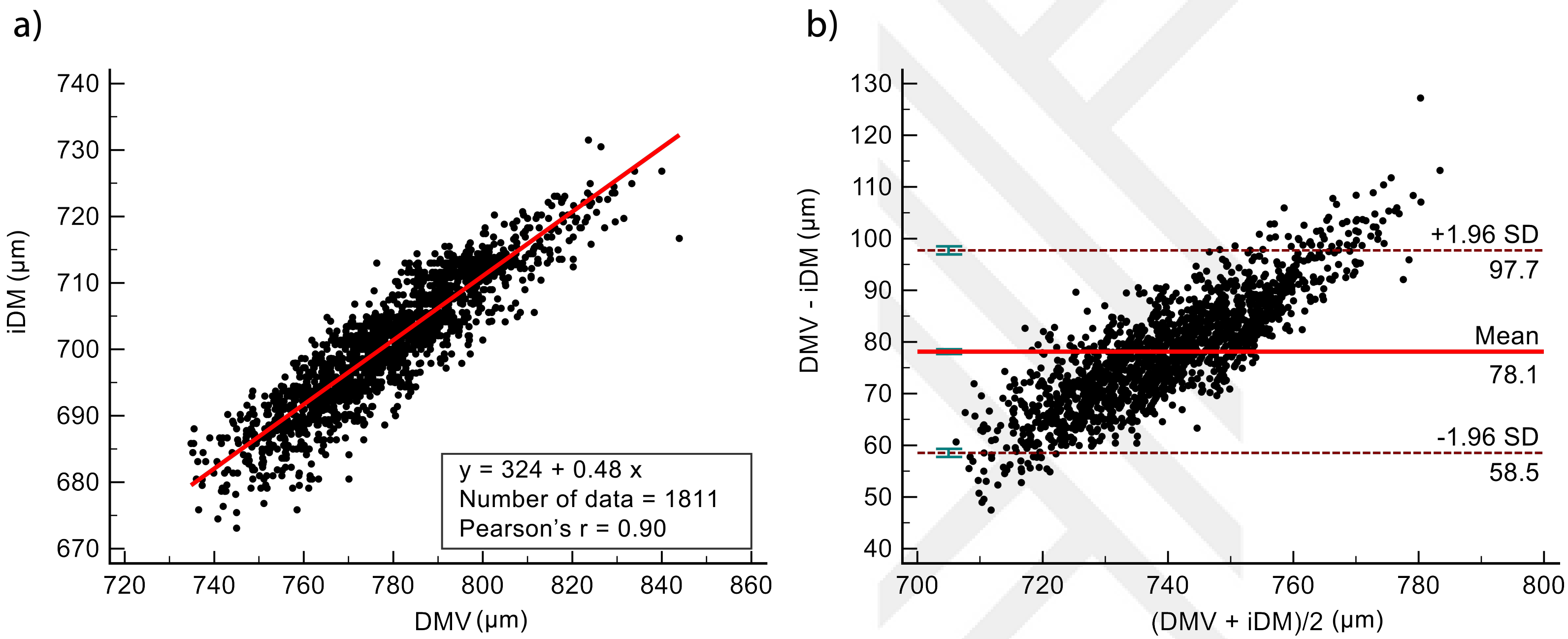

Figure 5.2: Comparison of droplet size measured by iDM and DMV. (a) Scatter plot of the data to check the evaluation of similarity. (b) Bland-Altman plot of the same data for evaluation of agreement analysis.

Table 5.1: Evaluation of similarity analysis between iDM and DMV.

Metric	Value
Fixed bias	324
Proportional (or scale) bias	0.48
Precision ratio	3.5
Squared sensitivity ratio	0.8

and 321.72, respectively. Plugging these values into the above equation, precision ratio of $\lambda = 3.50$ is obtained; which is an indicator of higher precision of iDM in comparison to DMV.

For sensitivity comparison of two methods, squared sensitivity ratio is used, which is defined as,

$$\gamma^2 = \frac{(sensitivity\ of\ method\ 2)^2}{(sensitivity\ of\ method\ 1)^2} = \frac{\beta_1^2/\sigma_{e2}^2}{1/\sigma_{e1}^2} = \beta_1^2\frac{\sigma_{e1}^2}{\sigma_{e2}^2} = \beta_1^2\lambda \tag{5.2}$$

Multiplying the proportional bias β_1 by precision, yields $\gamma^2 = 0.80$. Sensitivity ratio less than one indicates that DMV is more sensitive than iDM.

As seen in this analysis, iDM has higher droplet size measurement precision but less sensitivity in comparison to DMV. Further, Figure 5.2 (a) indicate Pearson's r value between iDM and DMV as 0.90, which is accepted as a very high correlation [90]. Evaluation of similarity results are summarized in Table 5.1.

Figure 5.2 (b) depicts a Bland-Altman plot of measurements. The most important conclusion of a Bland-Altman analysis is the interchangeability of the methods, which is determined based on the limits of agreement, ±1.96 SD boundaries, and tolerance. The limits of agreement in Figure 5.2 (b) are 58.5 μm and 97.7 μm that yields a 39.2 μm difference. Therefore, whenever the tolerance is over 39.2 μm, iDM and DMV can be used interchangeably.

There are two possible kinds of error in method comparison called constant bias and proportional bias. Constant bias occurs when the mean of differences in difference plot (Bland-Altman plot) is non-zero, and the proportional error happens when the differences tend to increase proportionally with the increasing average of measurements. The proportional error is a cause of slope in difference plot. Herein, the difference of mean from zero line, 78.1 μm, is equal to the constant bias. Yet, there is also a proportional error in size measurement. Clearly, differences tend to increase linearly as droplet size increases that is an indicator of increasing random error with increasing droplet size. The appeared linear trend can be caused by both unequal proportional biases and unequal precisions in two methods. To remove the linear trend generally there are two methods suggested. The first method is using a relative difference plot. Relative difference plot is similar to Bland-Altman difference plot, but the vertical axis is the difference divided by the average of two methods. The second method is using natural logarithm transformation of the differences against the average of two methods. Both approaches were unsuccessful in removing the linear trend in data.

iDM can calculate length, cap length, and velocity of each droplet. Droplet size ($L + 2CL$) is verified using a detailed method comparison analysis, however, droplet cap length and velocity comparison between the electrical and the image processing detection methods have not performed. None of the image processing tools (DMV or ADM) are providing droplet cap length. Although they do provide droplet velocity results, there is a subtle difference between the velocity measurements performed in image processing methods and our method. DMV and ADM measure velocity by analyzing successive frames that capture the droplet under test within the region of interest and provide an average velocity for the corresponding frames. However, iDM provides a more instantaneous-like velocity measurement. The measurement domain of iDM is defined by the electrode sensing region, which is much shorter. It should also be noted that droplet velocity changes continuously due to the pressure fluctuations during droplet formation and droplet maneuvering inside the main microchannel [91–93]. Hence, iDM is more successful in capturing the effects of such dynamic short-range events on droplet velocity. Furthermore, increasing droplet size requires an increase in the analysis region for image-processing methods, which would, in turn, increase the analysis time. Contrarily, iDM velocity measurement is not affected by the droplet length as long as the length is larger than the sensing region.

Chapter 6

Experimental Studies Using iDM

This chapter provides all the experimental studies that have used iDM. The first part is an application of iDM to investigate response of flow sources during droplet generation. In this way, iDM functionality was tested and provided new insights of flow sources. Second part of this chapter investigates effective parameters on droplet generation while using pressure flow source. Inspired from electronic evaluation boards, an evaluation chip was fabricated to explore all the factors and their effects on coefficient of variation of droplet size using design of experiment (DoE) methodology.

6.1 Response Time of Syringe Pump vs Pressure Pump

To demonstrate the use of iDM for real-time droplet formation analysis, the response time of systems driven by syringe pump and pressure pump were compared. Unarguably, syringe (displacement) and pressure pumps are the two most commonly used pumps in microfluidic systems.

It is shown that syringe pump has periodic fluctuations mainly due to the

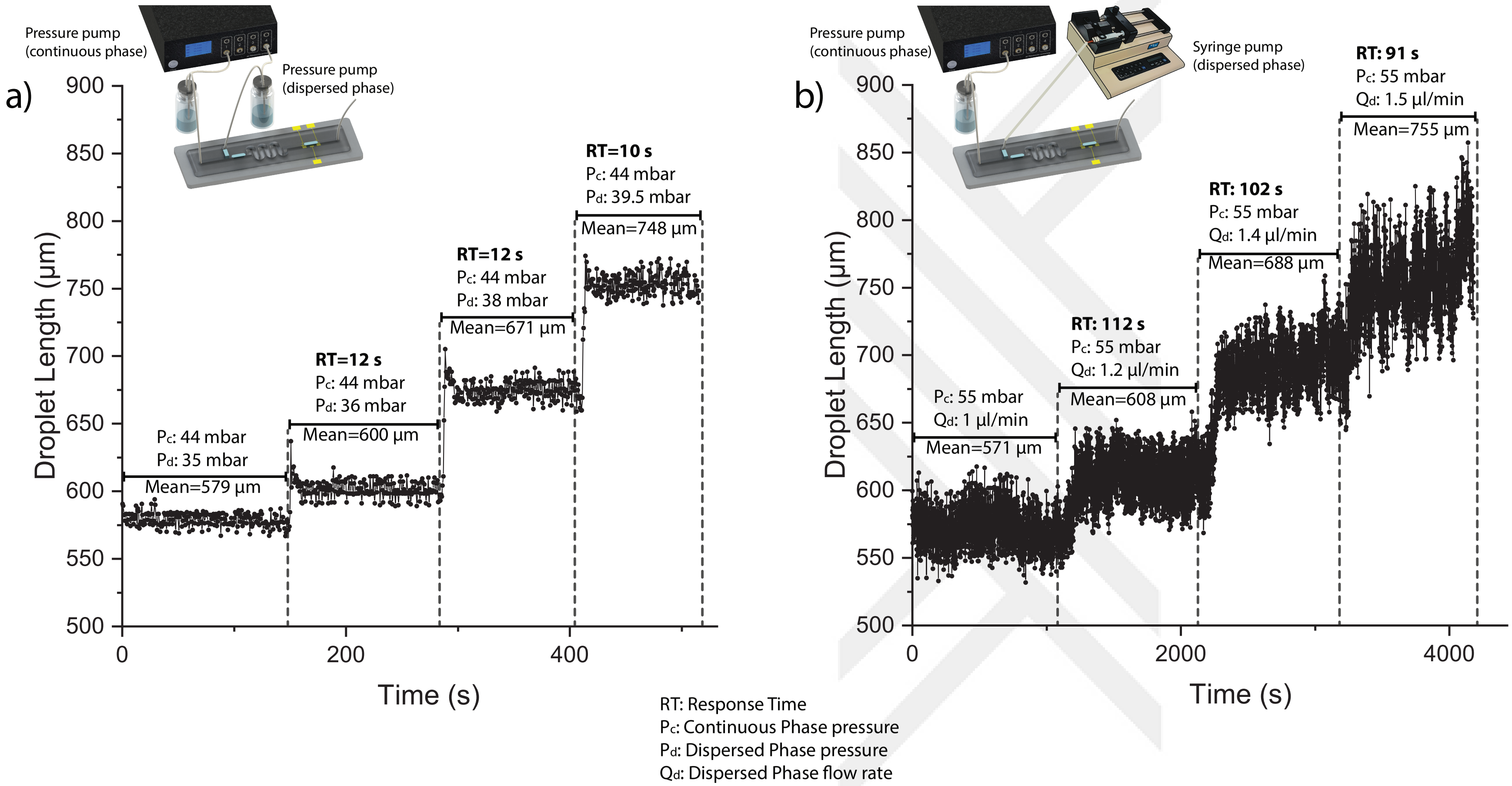

Figure 6.1: Droplet generation in different droplet length scales using different flow suppliers. (a) Pressure pump is used both for continuous phase and dispersed phase. (b) Pressure pump and syringe pump are used for continuous phase and dispersed phase, respectively.

stepper motor which pushes the plunger [94]. One of the parameters determining the oscillation periodicity of syringe pump driven flow is the syringe diameter and flow rate [94]. Flow fluctuations also affect pump response time that leads to various response times ranging from about two minutes to nearly one hour, reported by different studies [91, 94, 95]. Pressure pump has generally yielded better performance in terms of response time and flow fluctuations in comparison with syringe pump [94], [95]. Deciphering the cause of parameters affecting the response time of the system remains difficult due to the lack of a real-time analysis tool.

For the comparison of the response time, a high-end syringe pump (KDScientific 270) and pressure pump (Elveflow OB1) were used. The schematics of the two setups are given in Figure 6.1. For ease of comparison, continuous phase was supplied using the pressure pump for both experiments. For the first scenario, the dispersed phase was introduced using a pressure pump. The droplet size was modified by gradually increasing the pressure levels ($\mathrm{P_c}$, $\mathrm{P_d}$) that gave a step-wise droplet length response as a function of time, as shown in Figure 6.1 (a). The corresponding pressure levels and the mean droplet length for each setting are displayed on the figure. For each level, 200 droplets were formed and measured their length in real-time using iDM after which the input pressure levels are changed. As seen from these results when a pressure pump is used the response time is measured as around 12 s, for a system with approximately 1 Hz droplet generation rate.

A similar experiment was performed when the dispersed phase was supplied by the syringe pump. The continuous phase pressure ($\mathrm{P_c}$) was kept fixed at 55 mbar, whereas the syringe pump flow rate ($\mathrm{Q_d}$) is increased gradually from 1 to 1.5 µl/min to match the droplet lengths obtained in the first experiment. As seen from the results given in Figure 6.1 (b), an order of magnitude increase in the response time was observed, which is around 100 s. It is important to note that more than 1500 droplets were analyzed at each set due to the much longer response time of the syringe pump.

Similar results using two other models of syringe pumps have been obtained and concluded that the response time of syringe pumps are markedly lower than the pressure pump. Obtaining the same droplet length for multiple experiments was extremely challenging and it is needed to tailor the pump settings while observing the real-time droplet length measured by iDM. In such scenarios, iDM will be an enabling tool by its real-time droplet measurement capability, which can allow researchers to fine-tune their systems and easily differentiate between the warm-up and the steady-state droplet generation regimes.

6.2 Monodispersity Evaluation Chip

Investigation of various effects that are affecting microfluidic droplet monodispersity is of significant importance. Inspired by electrical evaluation chips, a droplet monodispersity evaluation chip is designed to investigate all main factors that are affecting this phenomenon. Utilizing a Design of Experiment (DoE) methodology, factors with a significant effect on droplet size monodispersity were determined in an experimental way. Following sections cover the fundamentals of Design of Experiment (DoE), experimental results, and DoE analysis.

6.2.1 Design of Experiments

One of the well-known approaches in the design of experiments is the one-factor at a time or one variable at a time (OFAT/OVAT), where one parameter varies at a time while keeping all the remaining parameters fixed so that effect of the parameter on the response is tested. This type of experimentation will yield results to some extent; however, it requires a large number of experiments while providing a limited amount of information. OFAT experiments give an understanding of the parameter effect at a fixed condition and are not able to provide information about interactions between parameters [96–98]. In the OFAT method, it is assumed that the effect of all parameters on the response is the same at different levels of other factors. Whenever this assumption turns wrong, we have to consider interactions of parameters as well.

Several experimental designs are currently available which are developed for various applications with specific requirements. Basic terms and fundamentals of DoE are explained in this section, to some extent, to give a basic understanding of the topic. An interested reader may refer to Design and Analysis of Experiments [98].

6.2.1.1 Basic Terms

This part provides basic terms that are being used in DoE to introduce the terminology used in this field (adopted from [97]).

Analysis of variance (ANOVA): A statistical method to evaluate the significance of the experiment results.

Effect: The change in response due to level change in a factor.

Factor: Independently controllable parameters that cause a change in the response.

Interaction: The change in response due to the combined change in two or more factors.

Level: Setting of a factor in an experiment.

Response: Output(s) of an experiment.

6.2.1.2 Full Factorial Design

Factorial designs are widely accepted both in industry and academia as the common DoE at two or three levels. Generally, full-factorial and fractional factorial designs are utilized. A general full factorial design consists of at least two factors, each at two levels least. In full factorial approach, all the possible combinations of the factors at each level should be conducted. Fractional factorial design basically takes a fraction of full factorial design and estimates the response in missing fractions. Although this method reduces the cost of experiments, its resolution is less than full factorial designs. One of the functional features of factorial designs is their ability in revealing interactions effect on the response, however, fractional factorial designs can provide fewer interaction effects than full factorial designs. This study has employed a full factorial design approach to precisely monitor the effects of factors on the response. Further, the design plan is randomized to reduce systematic mishap effects on the response.

Given a factors, and the i-th factor having b_i level, n number of the experiments in a full factorial design is yielded as,

$$n = \prod_{i=1}^{a} b_i \tag{6.1}$$

Thus, for an experiment with three factors at three levels 27 experiments are required. Full factorial experiment design cube plot for three experiments at three levels is illustrated in Figure 6.2. Spheres on each corner represent the combination of the factors and levels. On each plane of the cube, levels of two factors change in representative directions.

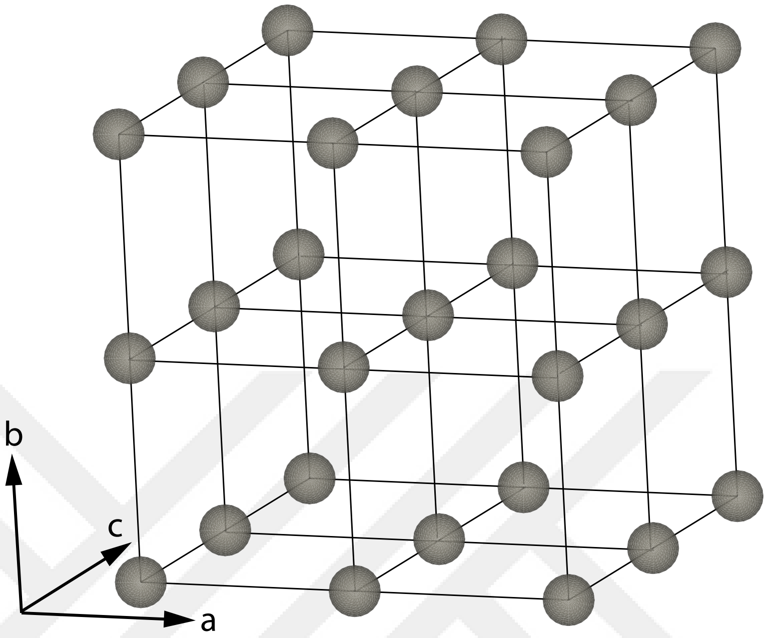

Figure 6.2: Full factorial experiment design cube for three factors at three levels.

6.2.2 Experimental

Microfluidic chip for monodispersity evaluation is designed to experimentally investigate how inlet pressure (P_{in}), main channel length resistance (R_m) (part of the channel that droplets are being generated and moved) and dispersed phase to continuous phase channel resistance ratio (R_d/R_c) would affect droplet monodispersity.

Experiments were planned using full-factorial design, in three levels. Analysis Of Variance (ANOVA) is carried out to fit a regression model. Analyzing full-factorial design, the most effective factors and their levels were detected. Understanding the effective factors on droplet length CV, contributes to monodisperse droplet generation.

6.2.2.1 Chip Design

Using DoE method for droplet monodispersity evaluation requires having a chip that can manipulate the factors of interest simultaneously on a single chip. The microfluidic chip needed for droplet monodispersity evaluation is designed in a way to explore P_{in}, R_m, and R_d/R_c effects on droplet generation. Actual masks used for soft lithography of microchannels and microelectrodes are depicted in Figure B.1 and B.2, respectively.

Using a pressure source controller, P_{in} is the easiest factor to be controlled. To control R_m, a microfluidic chip with six outlets was designed, as depicted in Figure 6.3. During the experiments, all the outlets except one, were blocked using a metal tip filled with cured PDMS. In this way, droplet channel length was controlled in a discrete manner. In this design, R_m increases with the increasing number of outlets, indicating that they have a linear relation.

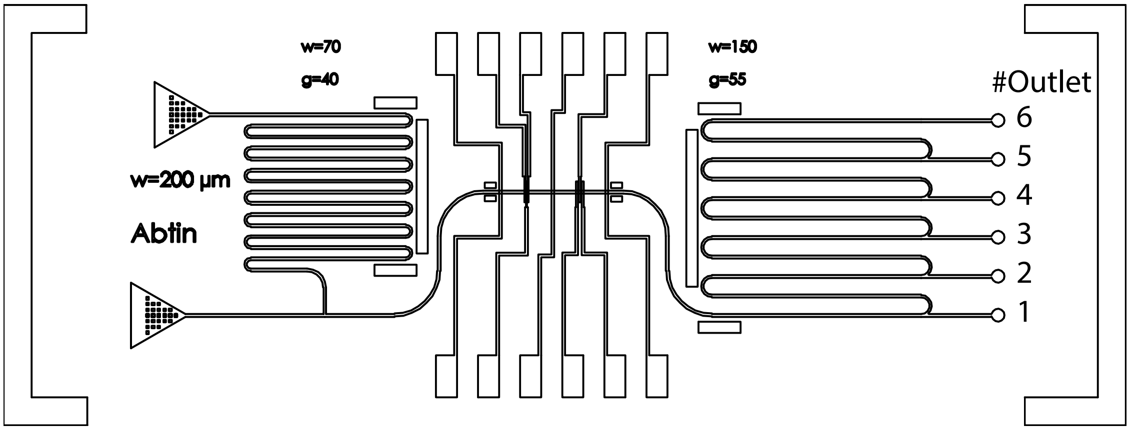

Figure 6.3: Microfluidic droplet size monodispersity evaluation chip design; consisting of microfluidic channels and microelectrodes design.

For manipulation of R_d/R_c, utilizing separate channel design approach is not feasible during the experiments, either for dispersed or continuous phase channels. To overcome this issue, TWIST valve is employed to change dispersed phase channel resistance. Although employing TWIST valve changes R_d/R_c in a linear manner, the exact value of the resistance is unknown. Furthermore, for the case of droplet channel resistance, increasing droplet channel length would increase hydrodynamic resistance, yet, the exact value of the hydrodynamic resistance is also dependent on the viscosity of the fluids and number of the droplets that are present inside the channel at the same time that the droplet is being generated. Therefore, despite not having the exact values for $\mathrm{R_m}$, and $\mathrm{R_d/R_c}$, these factors are manipulated using outlets and TWIST valve in three levels to investigate increasing/decreasing effect of each factor. Hereafter, state of the outlets and TWIST valve are representing $\mathrm{R_m}$, and $\mathrm{R_d/R_c}$, respectively.

High, middle and low levels of $\mathrm{P_{in}}$, $\mathrm{R_m}$, and $\mathrm{R_d/R_c}$ are opted in a way that droplets in all experimental sets were within the detectable range of iDM. Factors and levels used in the experiment are summarized in Table 6.1.

Table 6.1: Factors and their levels used during droplet generation.

	$\mathrm{P_{in}}$	$\mathrm{R_m}$	$\mathrm{R_d/R_c}$
Low	360 mbar (P_{360})	Outlet 3 (R_{m3})	Valve positioned in 0° (R_d/R_{c_0})
Middle	400 mbar (P_{400})	Outlet 4 (R_{m3})	Valve positioned in 90° (R_d/R_{c_90})
High	440 mbar (P_{440})	Outlet 5 (R_{m3})	Valve positioned in 180° (R_d/R_{c_180})

As can be seen in Figure 6.3, the impedimetric sensing region is positioned in the center of the chip. Microelectrode width and gap are 70 μm and 40 μm, respectively. Smaller microelectrode dimensions are chosen to detect smaller droplets in size.

6.2.2.2 Full-Factorial Experiments

General full-factorial design is used due to its high resolution in monitoring factors and their interactions effect on response. Factors and their levels are outlined in Table 6.1 and the only system response that is analyzed is droplet length CV which is briefly stated as CV in the following sections. Having three factors in three levels makes twenty-seven experiments ($3^3 = 27$) to conduct. Note that each experiment is conducted with at least 500 droplets. Table 6.2 summarizes the results of all experiments.

Table 6.2: Full-factorial design results.

No.	R_{m} (Outlet)	P_{in} (mbar)	$R_{\mathrm{d}}/R_{\mathrm{c}}$ (Screw (°))	CV%	Mean Length (μm)
1	3	360	0	0.94	458.22
2	3	360	90	0.88	470.31
3	3	360	180	0.87	439.16
4	3	400	0	0.75	471.09
5	3	400	90	0.71	455.06
6	3	400	180	0.63	430.42
7	3	440	0	0.57	492.84
8	3	440	90	0.55	481.55
9	3	440	180	0.52	448.81
10	4	360	0	0.92	459.41
11	4	360	90	0.90	435.27
12	4	360	180	0.89	401.62
13	4	400	0	0.74	468.39
14	4	400	90	0.70	454.67
15	4	400	180	0.65	425.22
16	4	440	0	0.67	495.82
17	4	440	90	0.65	479.51
18	4	440	180	0.54	443.55
19	5	360	0	1.19	442.29
20	5	360	90	1.11	426.59
21	5	360	180	1.01	400.9
22	5	400	0	1.02	455.26
23	5	400	90	1.06	431.92
24	5	400	180	0.79	402.59
25	5	440	0	0.71	462.13
26	5	440	90	0.68	448.74
27	5	440	180	0.63	418.18

6.2.3 Results and Discussions

All the experimental results given in Table 6.2 are analyzed in this section, using DoE analysis plots. Figure 6.4 presents the average effect of each main factor on droplet length CV. There are three points on each main effect plot that are representing the average of the response on a specific level of that effect. For a three factor in three level full factorial design, each point represents the average of nine experiments response. Main effects plot in Figure 6.4 reveals that increasing inlet pressure P_{in}, and R_d/R_c leads to a better droplet length CV, while increasing droplet channel length resistance R_m, has a negative effect.

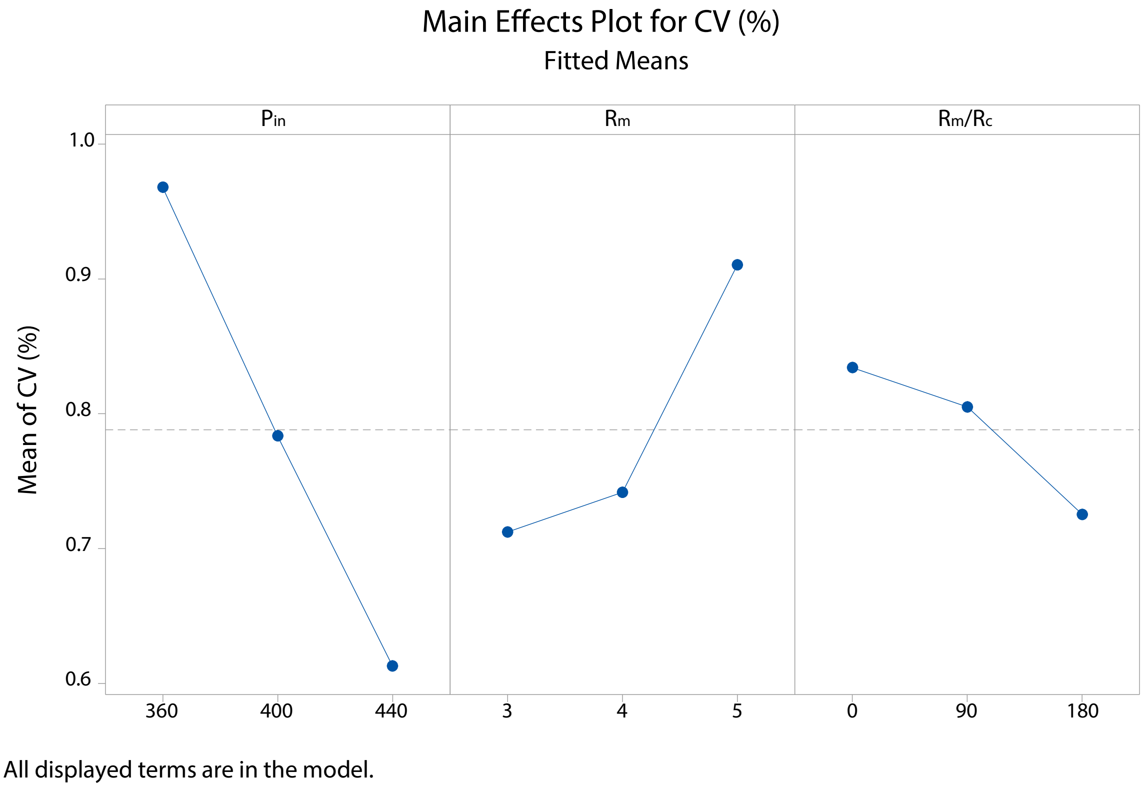

Figure 6.4: Main effects plot for droplet length CV.

One of the significant advantages of DoE is revealing interactions between several effects. Interactions happen whenever a factor is dependent on another factor change. Multi-Variable chart gives us all the information obtained from the main effects plot together with a visual interpretation of interaction among effects. The multi-variable chart is illustrated in Figure 6.5 to have a better understanding of the effect of all factors on the response of the system in each factor level. Figure 6.5 shows that as R_m increases there is a trend change in droplet length CV with different pressure levels. The trend change in pressure is a clear indicator of interaction between pressure and main channel length resistance.

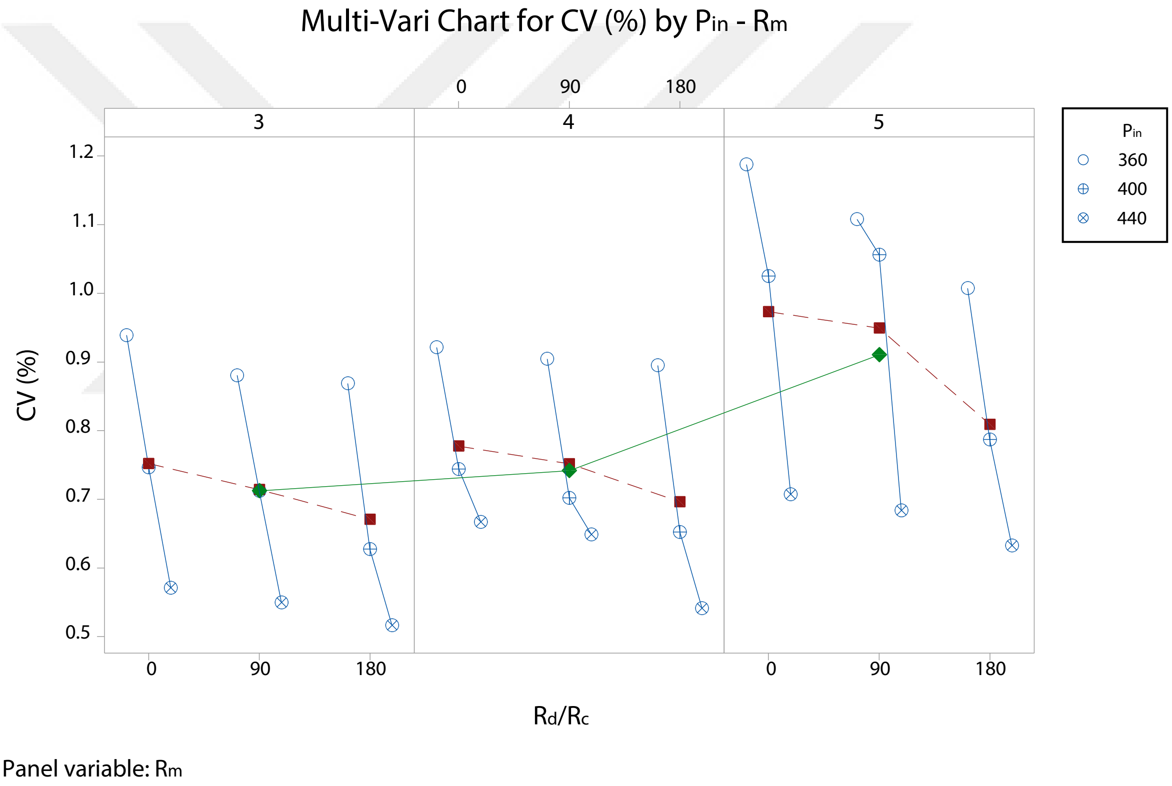

Figure 6.5: Multi-Variable chart for droplet length CV.

Interaction plot is a better way of visualizing interactions. The interaction plot for droplet length CV is illustrated in Figure 6.6. Each point depicts the average response for a combination of two factors. There would be no interaction if the lines had been in parallel. Interaction plot in Figure 6.6 confirms the P_{in} and R_m interaction which is observed in the multi-variable chart.

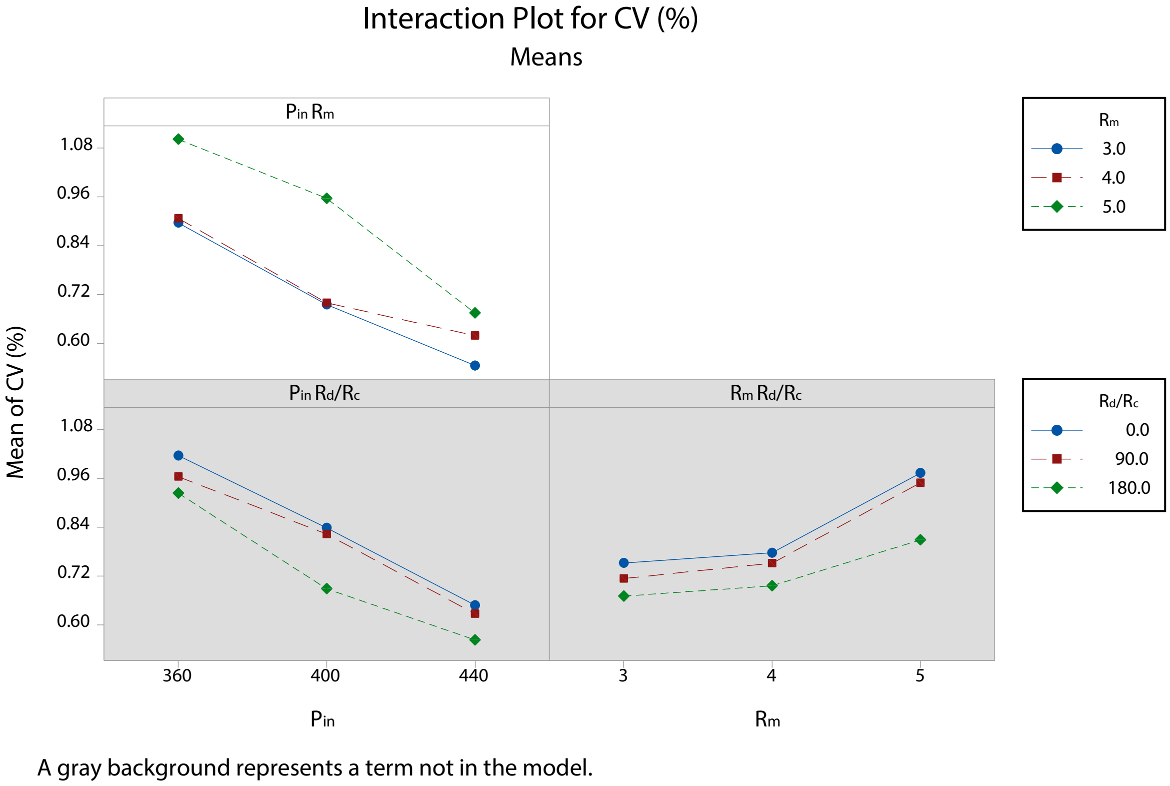

Figure 6.6: Interactions plot for droplet length CV.

Plots of main effects, multi-variable chart, and interactions of factors are presented, however, they cannot determine whether the factors have a significant effect on the response. P-value and α-value are used in determining the significance. Level of significance or α-value is the probability of a study that rejects the null-hypothesis. Whenever the probability of an occurrence is too small to happen by chance, it is called statistically significant. For instance, if a relation is significant given that α-value is set to 5%, it means that there is 95% probability that the relation would become true if the study is repeated. α-value is an arbitrary value that can be determined by our standards. Although α-value is an important parameter for rejecting the null-hypothesis, it cannot provide quantitative information on the level of significance. Therefore, P-value is commonly used to determine the significance level of the data [98].

ANOVA provides a mathematical model that relates factors to the response.

P-value that statistically reveals the significance of a factor effect on the response is also calculated in ANOVA. Further, ANOVA gives the F-value to compare variation between factor levels against variation within the levels. One can think of F-value as a signal-to-noise ratio. F-value becomes larger as differences in experiments increase, and decreases as variations increase [97].

In this study, using α-value of 0.15, ANOVA created a mathematical model for droplet size CV calculation using effects of the factors and their interactions, presented in equation 6.2. The absolute term is 0.78816. Second and third lines of the equation are the linear terms fitted to main effects. Remaining terms are interactions between $\mathrm{P_{in}}$ and $\mathrm{R_m}$.

$$
CV(\%) = \begin{aligned}[t]
&0.78816 \\
&- 0.0759\ R_{m3} -\ 0.0464\ R_{m4} +\ 0.1223\ R_{m5} \\
&+ 0.1798\ P_{360} -\ 0.0046\ P_{400} -\ 0.1752\ P_{440} \\
&+ 0.0460\ R_d/R_{c\_0} +\ 0.0168\ R_d/R_{c\_90} -\ 0.0629\ R_d/R_{c\_180} \\
&+ 0.0040\ R_{m3}P_{360} -\ 0.0124\ R_{m3}P_{400} +\ 0.0085\ R_{m3}P_{440} \\
&- 0.0146\ R_{m4}P_{360} -\ 0.0377\ R_{m4}P_{400} +\ 0.0524\ R_{m4}P_{440} \\
&+ 0.0107\ R_{m5}P_{360} +\ 0.0502\ R_{m5}P_{400} -\ 0.0608\ R_{m5}P_{440}
\end{aligned} \tag{6.2}
$$

Equation 6.2 is a linear regression fit for the data presented in Table 6.2. To control the quality of the regression equation, initially, it is required to check R-squared (R^2). R^2 is a measure of linear regression fit, which is in the range of $0 \leq R^2 \leq 1$. Higher R^2 values are always desirable since it is an indicator of less difference between data points and fitted line. However, attempts toward obtaining better fits may lead to the increasing number of terms in the regression model; because as number of independent variables increase, no matter if a chance correlation is added, always R^2 increases. Adjusted R-squared, $\mathrm{R^2}_{\mathrm{adj}}$, is used to overcome biased statistics of R^2. $\mathrm{R^2}_{\mathrm{adj}}$ value is independent of number of terms in the model and it only increases when a term improves the model and in a contrary situation the value decrease. There is also a measure to find out whether the regression model has a good prediction ability or not, that is called predicted R-squared, $\mathrm{R^2}_{\mathrm{pred}}$. Further insights of these measures are found in general statistic books [96–98].

In this study, R^2, $R^2{}_{adj}$, and $R^2{}_{pred}$ are calculated as 96.53%, 94.36%, and 90.12%, respectively. Outlined results in Table 6.3, are confirming the robustness of the model presented in equation 6.2.

Table 6.3: Regression model summary.

R^2	$R^2{}_{adj}$	$R^2{}_{pred}$
96.53%	94.36%	90.12%

Table 6.4 presents the ANOVA results. As it is earlier discussed, higher F-values indicate better model that is less prone to the variations. Generally, effects with P-values less than 0.05, and 0.01 are considered as significant, and highly significant, respectively.

Table 6.4: Analysis of Variance (ANOVA).

Source	F-Value	P-Value
Model	44.50	<0.01
Linear	71.34	<0.01
Outlet	53.05	<0.01
Pressure	146.21	<0.01
Valve	14.75	<0.01
2-Way Interactions	4.23	0.016
Outlet*Pressure	4.23	0.016

Both the main effects and interaction of the P_{in} and R_m have highly-significant and significant P-values, respectively. Also, the F-values are greater than unit, especially pressure P_{in} and R_m have the highest F-values, indicating less variation within the levels.

Finally, a Pareto chart is used to clearly visualize significant factors effecting the response together with their standardized effects, as illustrated in Figure 6.7. Pareto chart is a bar chart that consists of two axis. X-axis is the standardized effects (T-values) that are calculated in a T-test; and Y-axis is the factors that are sorted with their effects in a descending way. The baseline in Pareto chart functions as a border line that determines if a factor is significant and it is calculated using the α-value. Figure 6.7 demonstrates that $\mathrm{P_{in}}$, $\mathrm{R_m}$, $\mathrm{R_d/R_c}$, and interaction of $\mathrm{P_{in}}$ and $\mathrm{R_m}$ are the significant terms affecting the droplet length CV.

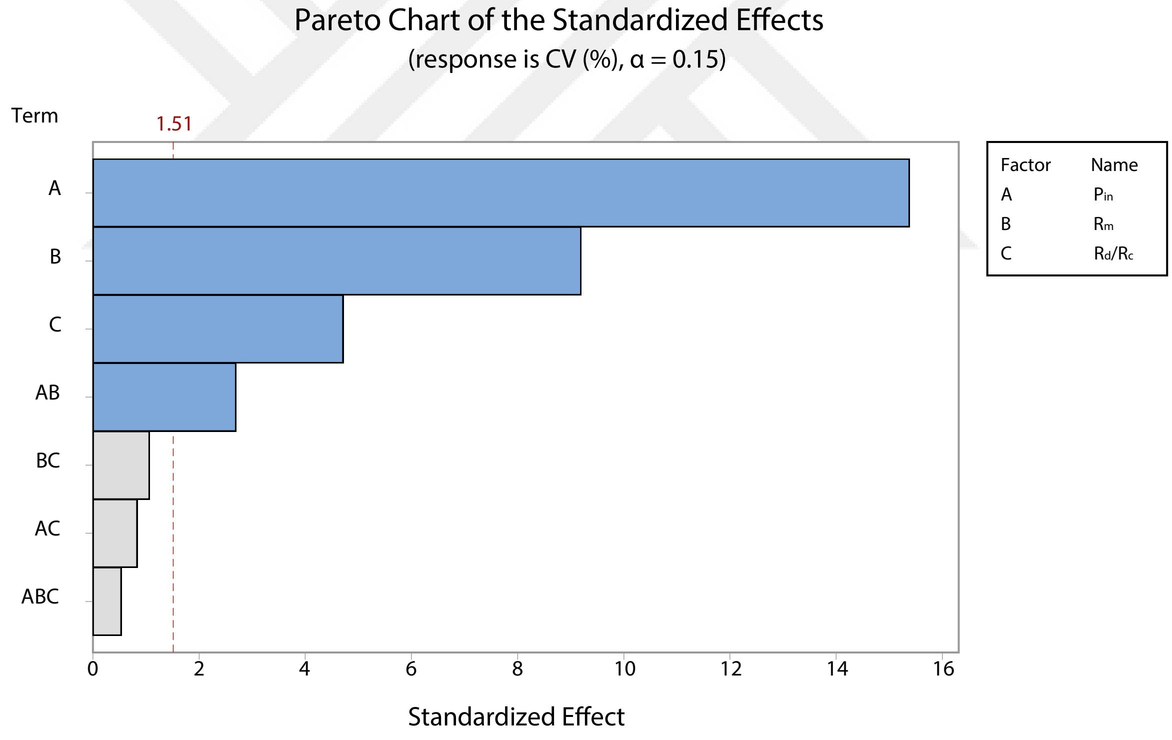
Pareto Chart of the Standardized Effects

(response is CV (%), $\alpha = 0.15$)

A gray bar represents a term not in the model.

Figure 6.7: Pareto chart of the standardized effects.

Exploiting DoE method in monodispersity evaluation chip has revealed three significant factors and their interactions effect on droplet length monodispersity. Experimental results unveiled that the inlet pressure, main channel length and hydrodynamic resistance ratio of the dispersed phase to continuous phase are the most important factors on droplet monodispersity, respectively. Moreover, the interaction of inlet pressure and the main channel length is another significant factor of droplet monodispersity that is first became clear in this study. Results of this study promote a fundamental improvement in microfluidic droplet generation. During monodispersity evaluation experiments, iDM has proven its practicality as a unique system for monitoring droplet physical properties in real-time. A large number of experiments with a considerable number of samples in each requires real-time measurement system. One of the most common uses of droplet-based microfluidic systems is biochemical synthesis, where repetitive experimentation with precise monitoring is a necessity.

6.3 Polyethylene Glycol (PEG) Synthesis

Droplet microfluidics has a variety of applications in biochemical synthesis which are mentioned in the introduction section. Considering the important factors in monodisperse microfluidic droplet generation, this study has proposed a system for monodisperse chemical particle synthesis. For a two-phase water-in-oil droplet generation, an aqueous solution of Poly(ethylene glycol) diacrylate (42.2% wt) together with its photo-initiator (2-Hydroxy-4′-(2-hydroxyethoxy)-2-methylpropiophenone) (3.7% wt) was prepared, and the continuous phase was silicon oil (100 cSt). Red food dye was added to improve visualization of PEG. Monodisperse droplets were generated and collected at the outlet of the microchannel into a soft Tygon tubing using a metal tip, shown in Figure 6.8.

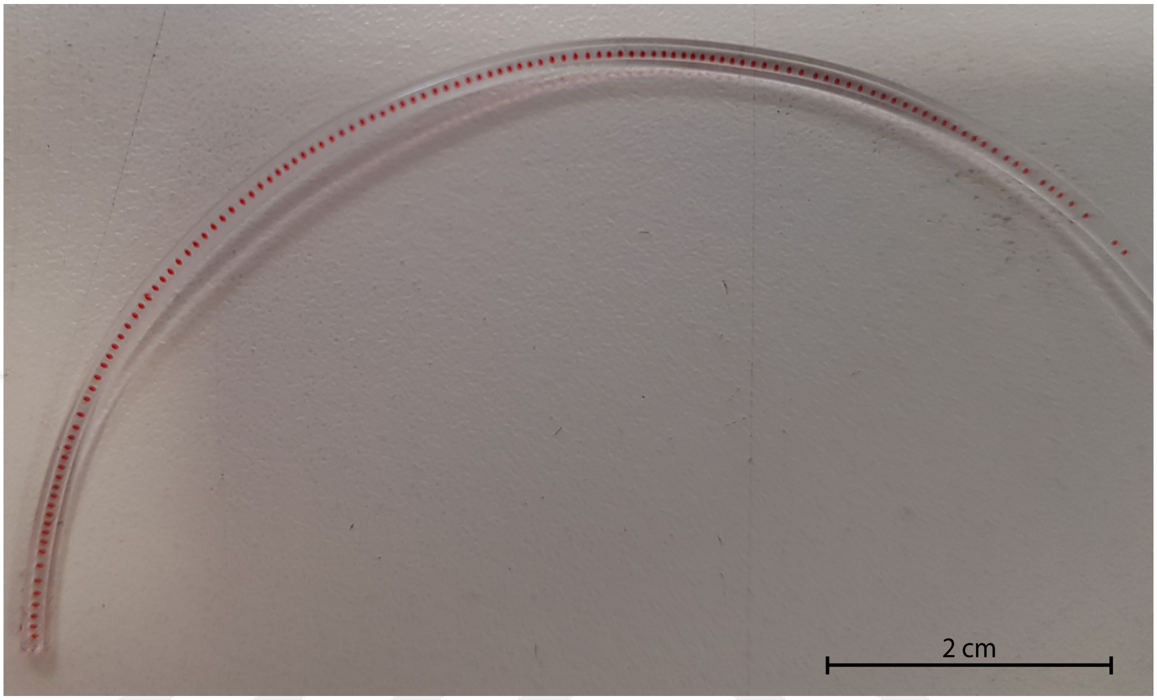

Figure 6.8: PEG microdroplets collected inside Tygon tubing.

A LED UV gun (Thor Labs, CS2010) was used to cure droplets inside the tubing, as they move into the Eppendorf tube. UV exposure for a second at 365 nm with 27 W/cm^2 is enough for solidification of each microdroplet. When pressures of the continuous phase and aqueous phase were set to 270 mbar and 180 mbar; spherical PEG particles with the average size of 180 μm were obtained, illustrated in Figure 6.9 (a). After washing processes due to water evaporation, volume shrinks to around 100 μm. Figure 6.9 depicts optical and SEM images of PEG particles.

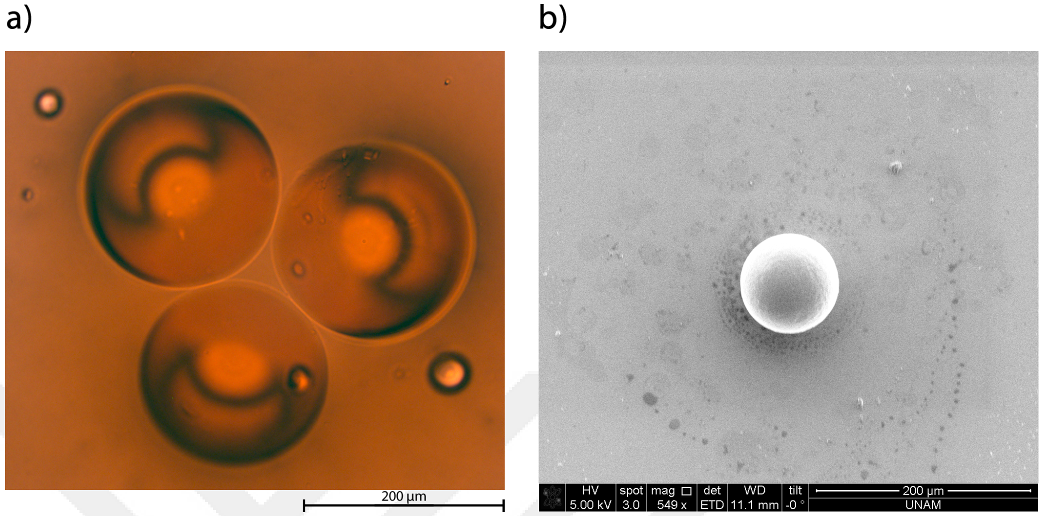

Figure 6.9: PEG microparticles under microscope. (a) PEG under optical microscope. (b) PEG under SEM.

Coefficient of variation in over 100 PEG particles, 1%, obtained from optical images is close to the coefficient of variation in droplet size, calculated by iDM as 0.95%. Further, size distribution of particles is the same as droplet size distribution with fixed bias of 10 μm that is due to the water evaporation and shrinkage in the size of PEG particles.

Monodisperse PEG particle synthesis demonstrates the significance of DoE analysis and real-time droplet monitoring system, iDM. Precise manipulation in droplet size by controlling pressures of both continuous phase and dispersed phase, give us a superior control in size control for biochemical synthesis, compared to bulk methods. iDM system not only monitors the droplets inside microchannel, it performs as a real-time system that gives us the final size distribution of synthesized chemicals.

Chapter 7

Conclusions and Future Perspectives

7.1 Conclusions

iDM offers the ability of real-time droplet morphology measurement of micro-droplets in microfluidic systems using an impedimetric measurement and micro-fabricated three coplanar electrodes. Droplet length, cap length, and velocity are derived from an analysis of electrical signal using finite element analysis. The optimized electrode geometry and more importantly the design procedures were developed for a large range of droplet length. An algorithm was developed to process the differential lock-in amplifier measurement in real-time and it functions without any lagging for throughputs up to 15000 droplet/s. A comparative study with an image-processing based detection method for droplet length yielded 0.90 Pearson's r correlation coefficient, 78.1 μm constant bias and 39.2 μm tolerance for interchangeability of the two methods. Syringe pump and pressure pump response time were compared using iDM that showed an order of magnitude difference for stable droplet generation in favor of pressure pump. Further, a droplet length monodispersity evaluation chip was designed to find out the underlying important factors behind droplet monodispersity using iDM. The most high-resolution method of DoE was utilized to investigate factors, interactions and effects of each. iDM provided a practical method for label-free droplets analysis, for a considerable number of experiments. Real-time signal processing, together with an easy-to-use interface, iDM has proven its capability in droplet analysis.

7.2 Future Perspectives

Although iDM has shown a great promise as a microfluidic droplet monitoring system, there are certain areas that can be improved. One possibility is to develop the system for detection and measurement of circular shaped objects. In spite of the simplicity of the software needed for this objective, the system needs to be optimized in a way that objects would move in the channel center in a focused manner. Such a system can significantly contribute to cytometry studies and microfluidic high-throughput droplet generation systems working with circular drops. In addition, iDM system can be used for analyzing electrical properties of droplets and particles to widen its applicability.

Moreover, iDM could be used in biochemical synthesis and analysis. Multi-stage multiplex assays such as Polymerase chain reaction (PCR) amplification is a possible important direction. Recently, droplet digital PCR (DD-PCR) technology has reduced traditional PCR costs. In DD-PCR, nano-liter droplets of water in oil form emulsions that each droplet is acting as a separate reaction chamber for PCR. Real-time monitoring is a must for such precise reactions; however, the microchannel surface chemistry should also be compatible with biochemical assays and optimized in a way that the electrical field can operate.

Bibliography

[1] R. Pethig and S. Smith, *Introductory Bioelectronics: For Engineers and Physical Scientists*. John Wiley & Sons, 2012.

[2] Y. Xia, E. Kim, X.-M. Zhao, J. A. Rogers, M. Prentiss, and G. M. Whitesides, "Complex Optical Surfaces Formed by Replica Molding Against Elastomeric Masters," *Science*, vol. 273, pp. 347–349, jul 1996.

[3] Y. Xia and G. M. Whitesides, "Soft Lithography," *Angewandte Chemie International Edition*, vol. 37, pp. 550–575, mar 1998.

[4] H. Wu, T. W. Odom, D. T. Chiu, and G. M. Whitesides, "Fabrication of complex three-dimensional microchannel systems in PDMS," *Journal of the American Chemical Society*, vol. 125, no. 2, pp. 554–559, 2003.

[5] C. S. Chen, D. N. Breslauer, J. I. Luna, A. Grimes, W. C. Chin, L. P. Lee, and M. Khine, "Shrinky-Dink microfluidics: 3D polystyrene chips," *Lab on a Chip*, vol. 8, pp. 622–624, mar 2008.

[6] H. Klank, J. P. Kutter, and O. Geschke, "CO2-laser micromachining and back-end processing for rapid production of PMMA-based microfluidic systems," *Lab on a Chip*, vol. 2, pp. 242–246, nov 2002.

[7] M. A. Unger, H. P. Chou, T. Thorsen, A. Scherer, and S. R. Quake, "Monolithic microfabricated valves and pumps by multilayer soft lithography," *Science*, vol. 288, pp. 113–116, apr 2000.

[8] M. B. Wabuyele, S. M. Ford, W. Stryjewski, J. Barrow, and S. A. Soper, "Single molecule detection of double-stranded DNA in poly(methylmethacrylate)

and polycarbonate microfluidic devices," *Electrophoresis*, vol. 22, pp. 3939–3948, oct 2001.

[9] P. S. Dittrich and A. Manz, "Lab-on-a-chip: Microfluidics in drug discovery," *Nature Reviews Drug Discovery*, vol. 5, no. 3, pp. 210–218, 2006.

[10] R. Riahi, A. Tamayol, S. A. M. Shaegh, A. M. Ghaemmaghami, M. R. Dokmeci, and A. Khademshosseini, "Microfluidics for advanced drug delivery systems," *Current Opinion in Chemical Engineering*, vol. 7, pp. 101–112, 2015.

[11] M. Zagnoni and J. M. Cooper, "Droplet microfluidics for high-throughput analysis of cells and particles," *Methods in Cell Biology*, vol. 102, pp. 23–48, 2011.

[12] M. Takinoue and S. Takeuchi, "Droplet microfluidics for the study of artificial cells," *Analytical and Bioanalytical Chemistry*, vol. 400, no. 6, pp. 1705–1716, 2011.

[13] H. N. Joensson and H. Andersson Svahn, "Droplet microfluidics-A tool for single-cell analysis," *Angewandte Chemie - International Edition*, vol. 51, pp. 12176–12192, dec 2012.

[14] K. F. Lei, Z. M. Wu, and C. H. Huang, "Impedimetric quantification of the formation process and the chemosensitivity of cancer cell colonies suspended in 3D environment," *Biosensors and Bioelectronics*, vol. 74, pp. 878–885, dec 2015.

[15] F. T. van den Brink, E. Gool, J. P. Frimat, J. Bomer, A. van den Berg, and S. Le Gac, "Parallel single-cell analysis microfluidic platform," *Electrophoresis*, vol. 32, pp. 3094–3100, nov 2011.

[16] Y. Zhang and H. R. Jiang, "A review on continuous-flow microfluidic PCR in droplets: Advances, challenges and future," *Analytica Chimica Acta*, vol. 914, pp. 7–16, mar 2016.

[17] Y. Zhang and P. Ozdemir, "Microfluidic DNA amplification-A review," *Analytica Chimica Acta*, vol. 638, pp. 115–125, apr 2009.

[18] S. Park, Y. Zhang, S. Lin, T. H. Wang, and S. Yang, "Advances in microfluidic PCR for point-of-care infectious disease diagnostics," *Biotechnology Advances*, vol. 29, pp. 830–839, nov 2011.

[19] M. A. Burns, B. N. Johnson, S. N. Brahmasandra, K. Handique, J. R. Webster, M. Krishnan, T. S. Sammarco, P. M. Man, D. Jones, D. Heldsinger, C. H. Mastrangelo, and D. T. Burke, "An integrated nanoliter DNA analysis device," *Science*, vol. 282, pp. 484–487, oct 1998.

[20] J. S. Marcus, W. F. Anderson, and S. R. Quake, "Parallel picoliter RT-PCR assays using microfluidics," *Analytical Chemistry*, vol. 78, no. 3, pp. 956–958, 2006.

[21] D. Erickson, X. Liu, U. Krull, and D. Li, "Electrokinetically controlled DNA hybridization microfluidic chip enabling rapid target analysis," *Analytical Chemistry*, vol. 76, no. 24, pp. 7269–7277, 2004.

[22] Y. He, M. Tsutsui, C. Fan, M. Taniguchi, and T. Kawai, "Gate manipulation of DNA capture into nanopores," *ACS Nano*, vol. 5, no. 10, pp. 8391–8397, 2011.

[23] K. F. Lei, Y. H. Wang, H. Y. Chen, J. H. Sun, and J. Y. Cheng, "Electrokinetic acceleration of DNA hybridization in microsystems," *Talanta*, vol. 138, pp. 149–154, jun 2015.

[24] A. H. Diercks, A. Ozinsky, C. L. Hansen, J. M. Spotts, D. J. Rodriguez, and A. Aderem, "A microfluidic device for multiplexed protein detection in nano-liter volumes," *Analytical Biochemistry*, vol. 386, pp. 30–35, mar 2009.

[25] D. Yang, X. Niu, Y. Liu, Y. Wang, X. Gu, L. Song, R. Zhao, L. Ma, Y. Shao, and X. Jiang, "Electrospun Nanofibrous Membranes: A Novel Solid Substrate for Microfluidic Immunoassays for HIV," *Advanced Materials*, vol. 20, pp. 4770–4775, dec 2008.

[26] A. Bhattacharyya and C. M. Klapperich, "Design and testing of a disposable microfluidic chemiluminescent immunoassay for disease biomarkers in human serum samples," *Biomedical Microdevices*, vol. 9, pp. 245–251, apr 2007.

[27] A. E. Herr, A. V. Hatch, D. J. Throckmorton, H. M. Tran, J. S. Brennan, W. V. Giannobile, and A. K. Singh, "Microfluidic immunoassays as rapid saliva-based clinical diagnostics," *Proceedings of the National Academy of Sciences*, vol. 104, pp. 5268–5273, mar 2007.

[28] S. Xu, Z. Nie, M. Seo, P. Lewis, E. Kumacheva, H. A. Stone, P. Garstecki, D. B. Weibel, I. Gitlin, and G. M. Whitesides, "Generation of monodisperse particles by using microfluidics: Control over size, shape, and composition," *Angewandte Chemie - International Edition*, vol. 44, no. 5, pp. 724–728, 2005.

[29] L. Shang, Y. Cheng, and Y. Zhao, "Emerging Droplet Microfluidics," *Chemical Reviews*, vol. 117, pp. 7964–8040, jun 2017.

[30] T. S. Kaminski and P. Garstecki, "Controlled droplet microfluidic systems for multistep chemical and biological assays," *Chemical Society Reviews*, vol. 46, no. 20, pp. 6210–6226, 2017.

[31] H. Song, D. L. Chen, and R. F. Ismagilov, "Reactions in droplets in microfluidic channels," *Angewandte Chemie - International Edition*, vol. 45, no. 44, pp. 7336–7356, 2006.

[32] T. M. Squires and S. R. Quake, "Microfluidics: Fluid physics at the nanoliter scale," *Reviews of Modern Physics*, vol. 77, pp. 977–1026, oct 2005.

[33] P. Gravesen, J. Branebjerg, and O. S. Jensen, "Microfluidics-a review," *Journal of Micromechanics and Microengineering*, vol. 3, pp. 168–182, dec 1993.

[34] M. Koch, D. Chatelain, A. G. R. Evans, and A. Brunnschweiler, "Two simple micromixers based on silicon," *Journal of Micromechanics and Microengineering*, vol. 8, pp. 123–126, jun 1998.

[35] Y. Song, C. S. S. R. Kumar, and J. Hormes, "Fabrication of an SU-8 based microfluidic reactor on a PEEK substrate sealed by a flexible semi-solid transfer (FST) process," *Journal of Micromechanics and Microengineering*, vol. 14, pp. 932–940, jul 2004.

[36] H. Kitahata, N. Yoshinaga, K. H. Nagai, and Y. Sumino, "Dynamics of Droplets," pp. 85–118, Berlin, Heidelberg: Springer Berlin Heidelberg, 2013.

[37] L. Shui, J. C. Eijkel, and A. van den Berg, "Multiphase flow in microfluidic systems - Control and applications of droplets and interfaces," *Advances in Colloid and Interface Science*, vol. 133, pp. 35–49, may 2007.

[38] C. N. Baroud, F. Gallaire, and R. Dangla, "Dynamics of microfluidic droplets," *Lab on a Chip*, vol. 10, pp. 2032–2045, jul 2010.

[39] H. A. Stone, "Dynamics of Drop Deformation and Breakup in Viscous Fluids," *Annual Review of Fluid Mechanics*, vol. 26, pp. 65–102, 1994.

[40] H. Song and R. F. Ismagilov, "Millisecond Kinetics on a Microfluidic Chip Using Nanoliters of Reagents," *Journal of the American Chemical Society*, vol. 125, no. 47, pp. 14613–14619, 2003.

[41] A. Ufer, D. Sudhoff, A. Mescher, and D. W. Agar, "Suspension catalysis in a liquid-liquid capillary microreactor," *Chemical Engineering Journal*, vol. 167, pp. 468–474, mar 2011.

[42] T. P. Lagus and J. F. Edd, "A review of the theory, methods and recent applications of high-throughput single-cell droplet microfluidics," *Journal of Physics D: Applied Physics*, vol. 46, p. 114005, mar 2013.

[43] O. J. Dressler, X. Casadevall i Solvas, and A. J. DeMello, "Chemical and Biological Dynamics Using Droplet-Based Microfluidics," *Annual Review of Analytical Chemistry*, vol. 10, no. 1, pp. 1–24, 2017.

[44] P. C. Gach, K. Iwai, P. W. Kim, N. J. Hillson, and A. K. Singh, "Droplet microfluidics for synthetic biology," *Lab on a Chip*, vol. 17, pp. 3388–3400, oct 2017.

[45] D. Dendukuri and P. S. Doyle, "The synthesis and assembly of polymeric microparticles using microfluidics," *Advanced Materials*, vol. 21, pp. 4071–4086, nov 2009.

[46] Y. Zhu and Q. Fang, “Analytical detection techniques for droplet microfluidics-A review,” *Analytica Chimica Acta*, vol. 787, pp. 24–35, jul 2013.

[47] A. Kalantarifard, A. Saateh, and C. Elbuken, “Label-Free Sensing in Microdroplet-Based Microfluidic Systems,” *Chemosensors*, vol. 6, no. 2, p. 23, 2018.

[48] T. Luo, L. Fan, R. Zhu, D. Sun, T. Luo, L. Fan, R. Zhu, and D. Sun, “Microfluidic Single-Cell Manipulation and Analysis: Methods and Applications,” *Micromachines*, vol. 10, p. 104, feb 2019.

[49] T. Sun and H. Morgan, “Single-cell microfluidic impedance cytometry: a review,” *Microfluidics and Nanofluidics*, vol. 8, pp. 423–443, apr 2010.

[50] P. K. Isgor, M. Marcali, M. Keser, and C. Elbuken, “Microfluidic droplet content detection using integrated capacitive sensors,” *Sensors and Actuators B: Chemical*, vol. 210, pp. 669–675, apr 2015.

[51] J. Z. Chen, A. A. Darhuber, S. M. Troian, and S. Wagner, “Capacitive sensing of droplets for microfluidic devices based on thermocapillary actuation,” *Lab on a Chip*, vol. 4, p. 473, oct 2004.

[52] C. Elbuken, T. Glawdel, D. Chan, and C. L. Ren, “Detection of microdroplet size and speed using capacitive sensors,” *Sensors and Actuators A: Physical*, vol. 171, no. 2, pp. 55–62, 2011.

[53] V. Jain, A. Hole, R. Deshmukh, and R. Patrikar, “Dynamic capacitive sensing of droplet parameters in a low-cost open EWOD system,” *Sensors and Actuators A: Physical*, vol. 263, pp. 224–233, aug 2017.

[54] N. Srivastava and M. A. Burns, “Electronic drop sensing in microfluidic devices: automated operation of a nanoliter viscometer,” *Lab on a Chip*, vol. 6, p. 744, may 2006.

[55] F. Wang and M. A. Burns, “Multiphase bioreaction microsystem with automated on-chip droplet operation,” *Lab on a Chip*, vol. 10, p. 1308, may 2010.

[56] M. C. Cole and P. J. Kenis, “Multiplexed electrical sensor arrays in microfluidic networks,” *Sensors and Actuators B: Chemical*, vol. 136, pp. 350–358, mar 2009.

[57] W. Engl, M. Roche, A. Colin, P. Panizza, and A. Ajdari, “Droplet traffic at a simple junction at low capillary numbers,” *Physical Review Letters*, vol. 95, no. 20, pp. 1–4, 2005.

[58] N. T. Nguyen, S. Lassemono, and F. A. Chollet, “Optical detection for droplet size control in microfluidic droplet-based analysis systems,” *Sensors and Actuators, B: Chemical*, vol. 117, no. 2, pp. 431–436, 2006.

[59] M. R. De Saint Vincent, S. Cassagnére, J. Plantard, and J. P. Delville, “Real-time droplet caliper for digital microfluidics,” *Microfluidics and Nanofluidics*, vol. 13, no. 2, pp. 261–271, 2012.

[60] Y. W. Hsieh, A. B. Wang, X. Y. Lu, and L. A. Wang, “High-throughput on-line multi-detection for refractive index, velocity, size, and concentration measurements of micro-two-phase flow using optical microfibers,” *Sensors and Actuators, B: Chemical*, vol. 237, pp. 841–848, 2016.

[61] G. Bettella, R. Zamboni, G. Pozza, A. Zaltron, C. Montevecchi, M. Pierno, G. Mistura, C. Sada, L. Gauthier-Manuel, and M. Chauvet, “LiNbO3 integrated system for opto-microfluidic sensing,” *Sensors and Actuators B: Chemical*, vol. 282, no. April 2018, pp. 391–398, 2019.

[62] S. U. Hassan, A. M. Nightingale, and X. Niu, “Optical flow cell for measuring size, velocity and composition of flowing droplets,” *Micromachines*, vol. 8, no. 2, pp. 1–10, 2017.

[63] S.-u. Hassan, A. M. Nightingale, and X. Niu, “Micromachined optical flow cell for sensitive measurement of droplets in tubing,” *Biomedical Microdevices*, vol. 20, no. 4, p. 92, 2018.

[64] A. G. Teixeira, M.-C. Tsai, and J. Frampton, “Microfluidic control of droplet formation from stable emulsions formed by aqueous two-phase systems,” *Microfluidics, BioMEMS, and Medical Microsystems XVI*, no. February 2018, p. 15, 2018.

[65] M. Chabert and J.-L. Viovy, “Microfluidic high-throughput encapsulation and hydrodynamic self-sorting of single cells,” *Proceedings of the National Academy of Sciences*, vol. 105, no. 9, pp. 3191–3196, 2008.

[66] M. Zantow, R. Dendere, and T. S. Douglas, “Image-based analysis of droplets in microfluidics,” *Proceedings of the Annual International Conference of the IEEE Engineering in Medicine and Biology Society, EMBS*, pp. 1776–1779, 2013.

[67] A. S. Basu, “Droplet morphometry and velocimetry (DMV): a video processing software for time-resolved, label-free tracking of droplet parameters,” *Lab on a Chip*, vol. 13, no. 10, pp. 1892–1901, 2013.

[68] Z. Z. Chong, S. B. Tor, A. M. Gañán-Calvo, Z. J. Chong, N. H. Loh, N. T. Nguyen, and S. H. Tan, “Automated droplet measurement (ADM): an enhanced video processing software for rapid droplet measurements,” *Microfluidics and Nanofluidics*, vol. 20, no. 4, pp. 1–14, 2016.

[69] A. M. Esmaeel, T. ElMelegy, and M. Abdelgawad, “Multi-purpose machine vision platform for different microfluidics applications,” *Biomedical Microdevices*, vol. 21, p. 68, sep 2019.

[70] X. Niu, M. Zhang, S. Peng, W. Wen, and P. Sheng, “Real-time detection, control, and sorting of microfluidic droplets,” *Biomicrofluidics*, vol. 1, no. 4, p. 44101, 2007.

[71] T. Dong and C. Barbosa, “Capacitance Variation Induced by Microfluidic Two-Phase Flow across Insulated Interdigital Electrodes in Lab-On-Chip Devices,” *Sensors*, vol. 15, no. 2, pp. 2694–2708, 2015.

[72] N. E. Yakdi, D. Bricault, F. Huet, and K. Ngo, “Detection and Sizing of Single Droplets Flowing in a Microfluidic Device by Impedance Measurement,” *Procedia Engineering*, vol. 168, pp. 1466–1470, 2016.

[73] H. Fu, W. Zeng, S. Li, and S. Yuan, “Electrical-detection droplet microfluidic closed-loop control system for precise droplet production,” *Sensors and Actuators A: Physical*, vol. 267, pp. 142–149, 2017.

[74] E. V. Moiseeva, A. A. Fletcher, and C. K. Harnett, "Thin-film electrode based droplet detection for microfluidic systems," *Sensors and Actuators B: Chemical*, vol. 155, no. 1, pp. 408–414, 2011.

[75] J. R. Macdonald, "Impedance spectroscopy," *Annals of Biomedical Engineering*, vol. 20, pp. 289–305, may 1992.

[76] Y. A. Djawad, J. Kiely, P. Wraith, and R. Luxton, "Lock-in Amplifier as a Sensitive Instrument for Biomedical Measurement : Analysis and Implementation," *TELKOMNIKA Indonesian Journal of Electrical Engineering*, vol. 12, no. 10, pp. 7214–7222, 2014.

[77] Keysight Technologies, "Impedance Measurement Handbook," p. 140, 2016.

[78] D. C. Duffy, J. C. McDonald, O. J. Schueller, and G. M. Whitesides, "Rapid prototyping of microfluidic systems in poly(dimethylsiloxane)," *Analytical Chemistry*, vol. 70, no. 23, pp. 4974–4984, 1998.

[79] S. Elizabeth Hulme, S. S. Shevkoplyas, and G. M. Whitesides, "Incorporation of prefabricated screw, pneumatic, and solenoid valves into microfluidic devices," *Lab on a Chip*, vol. 9, no. 1, pp. 79–86, 2009.

[80] P. Zhu and L. Wang, "Passive and active droplet generation with microfluidics: a review," *Lab on a Chip*, vol. 17, pp. 34–75, dec 2017.

[81] T. Glawdel, C. Elbuken, and C. L. Ren, "Droplet Generation in Microfluidics," in *Encyclopedia of Microfluidics and Nanofluidics*, pp. 1–12, Boston, MA: Springer US, 2013.

[82] D. G. Altman and J. M. Bland, "Measurement in Medicine: The Analysis of Method Comparison Studies," *The Statistician*, vol. 32, no. 3, pp. 307–317, 1983.

[83] P. K. Choudhary and H. N. Nagaraja, *Measuring Agreement Models, Methods, and Applications.* New York: John Wiley & Sons, 2017.

[84] J. M. Bland and D. G. Altman, "Measuring agreement in method comparison studies," *Statistical Methods in Medical Research*, vol. 8, no. 2, pp. 135–160, 1999.

[85] J. Martin Bland and D. G. Altman, “Statistical Methods for Assessing Agreement Between Two Methods of Clinical Measurement,” *The Lancet*, vol. 327, no. 8476, pp. 307–310, 1986.

[86] P. H. Petersen, D. Stöckl, O. Blaabjerg, B. Pedersen, E. Birkemose, L. Thienpont, J. F. Lassen, J. Kjeldsen, R. D. Group, and R. D. Group, “Graphical interpretation of analytical data from comparison of a field method with a Reference Method by use of difference plots,” *Clinical Chemistry*, vol. 43, pp. 2039–2046, nov 1997.

[87] M. A. Pollock, S. G. Jefferson, J. W. Kane, K. Lomax, G. MacKinnon, and C. B. Winnard, “Method Comparison—A Different Approach,” *Annals of Clinical Biochemistry*, vol. 29, pp. 556–560, sep 1992.

[88] K. Linnet and I. Bruunshuus, “HPLC with enzymatic detection as a candidate reference method for serum creatinine.,” *Clinical Chemistry*, vol. 37, pp. 1669–1675, oct 1991.

[89] J. R. Budd, A. P. Durham, T. E. Gwise, B. Iriarte, A. Kallner, K. Linnet, R. Magari, and J. E. Vaks, *Measurement procedure comparison and bias estimation using patient samples : approved guideline*. No. August, Wayne, PA: Clinical and Laboratory Standards Institute (CLSI), third edit ed., 2013.

[90] D. E. Hinkle, W. Wiersma, and S. G. Jurs, *Applied statistics for the behavioral sciences*. Houghton Mifflin, 2002.

[91] T. Glawdel and C. L. Ren, “Global network design for robust operation of microfluidic droplet generators with pressure-driven flow,” *Microfluidics and Nanofluidics*, vol. 13, no. 3, pp. 469–480, 2012.

[92] N. R. Beer, K. A. Rose, and I. M. Kennedy, “Observed velocity fluctuations in monodisperse droplet generators,” *Lab on a Chip*, vol. 9, no. 6, pp. 838–840, 2009.

[93] V. van Steijn, M. T. Kreutzer, and C. R. Kleijn, “Velocity fluctuations of segmented flow in microchannels,” *Chemical Engineering Journal*, vol. 135, no. SUPPL. 1, pp. 159–165, 2007.

[94] P. M. Korczyk, O. Cybulski, S. Makulska, and P. Garstecki, "Effects of unsteadiness of the rates of flow on the dynamics of formation of droplets in microfluidic systems," *Lab on a Chip*, vol. 11, no. 1, pp. 173–175, 2011.

[95] W. Zeng, I. Jacobi, D. J. Beck, S. Li, and H. A. Stone, "Characterization of syringe-pump-driven induced pressure fluctuations in elastic microchannels," *Lab on a Chip*, vol. 15, no. 4, pp. 1110–1115, 2015.

[96] J. Antony, *Design of Experiments for Engineers and Scientists*. Elsevier Ltd, 2003.

[97] M. J. Anderson and P. J. Whitcomb, *DOE Simplified - Practical Tools for Effective Experimentation*. CRC Press, 2007.

[98] D. C. Montgomery, *Design and analysis of experiments*. John Wiley & Sons, ninth ed. ed., 2017.

Appendix A

Droplet Length Simulations

Effect of varying electrode width and gap on signal amplitude has been investigated for droplet lengths in the range of 300 μm to 1500 μm, depicted in Figure A.1. The signal amplitude does not increase significantly for electrode widths over 150 μm, for droplet lengths over 500 μm. Hence, the system does not impose an upper limit for droplet length. The minimum droplet size can be determined based on such an analysis. The highest signal amplitude was obtained for the smallest electrode gap, which is chosen as 20 μm, in our analysis.

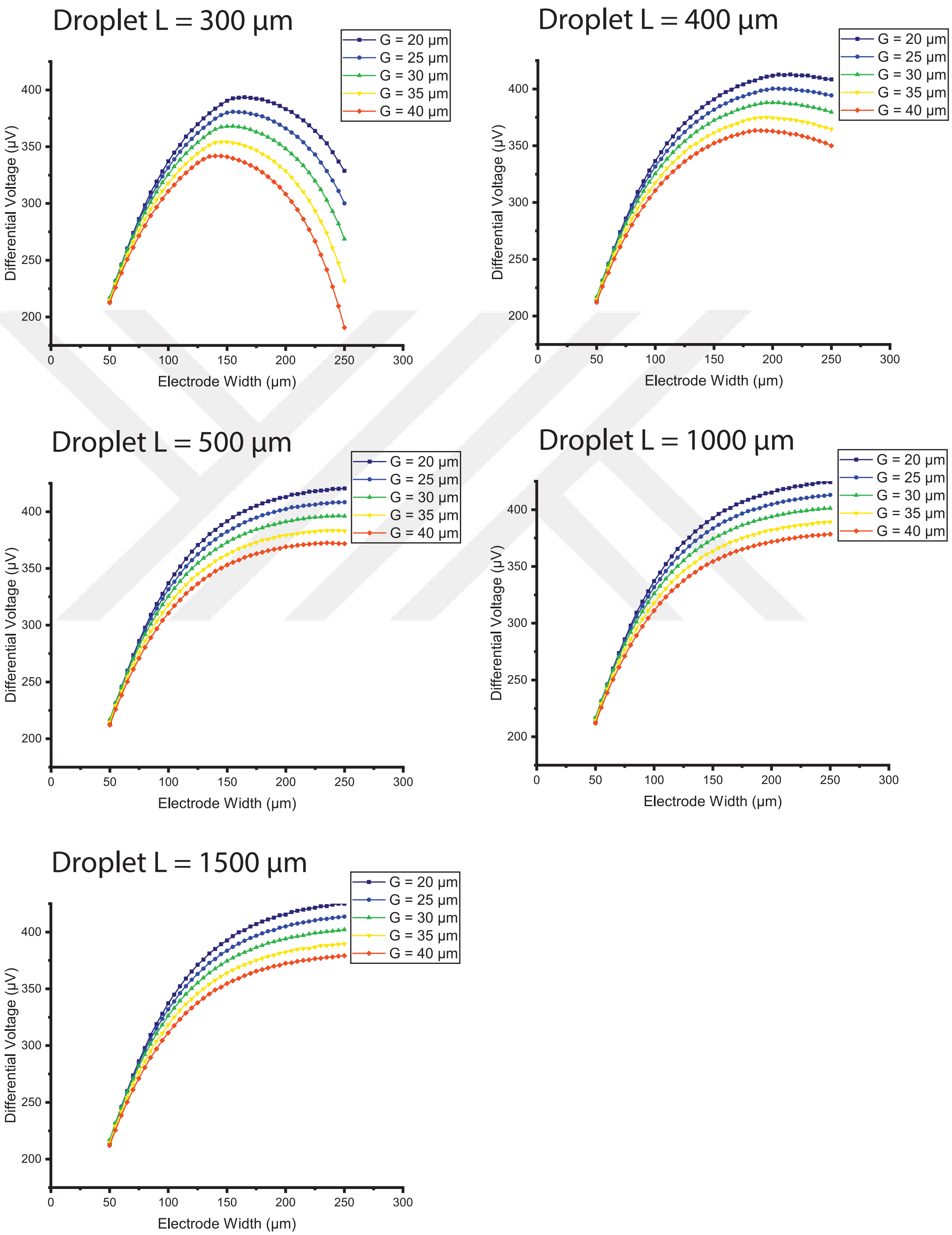

Figure A.1: Simulation results showing the signal amplitude for varying electrode geometries and droplet lengths.

Appendix B

Masks of the Microfluidic Chip

Figure B.1 and B.2 are presenting masks of microchannel mold and electrode that are designed for monodispersity evaluation chip.

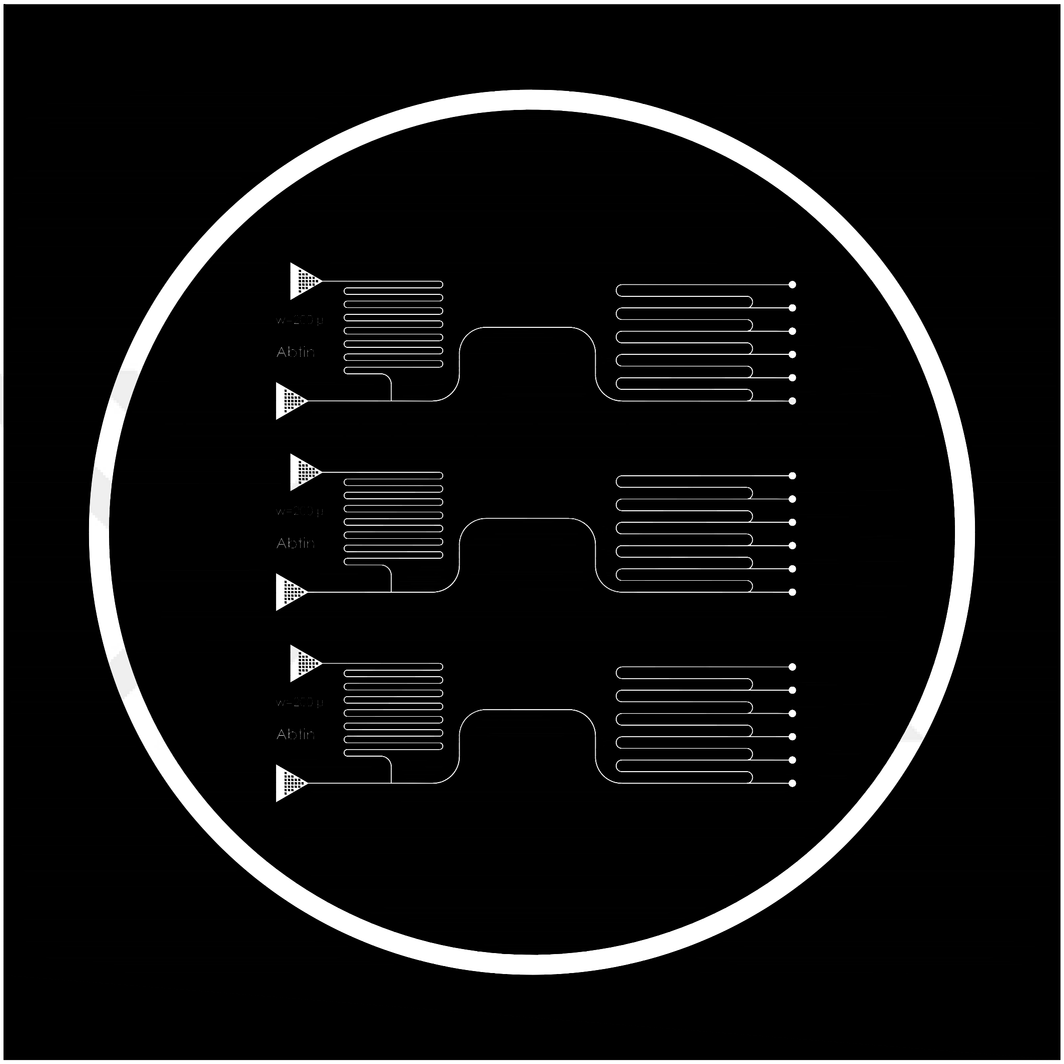

Figure B.1: Monodispersity evaluation chip mold mask.

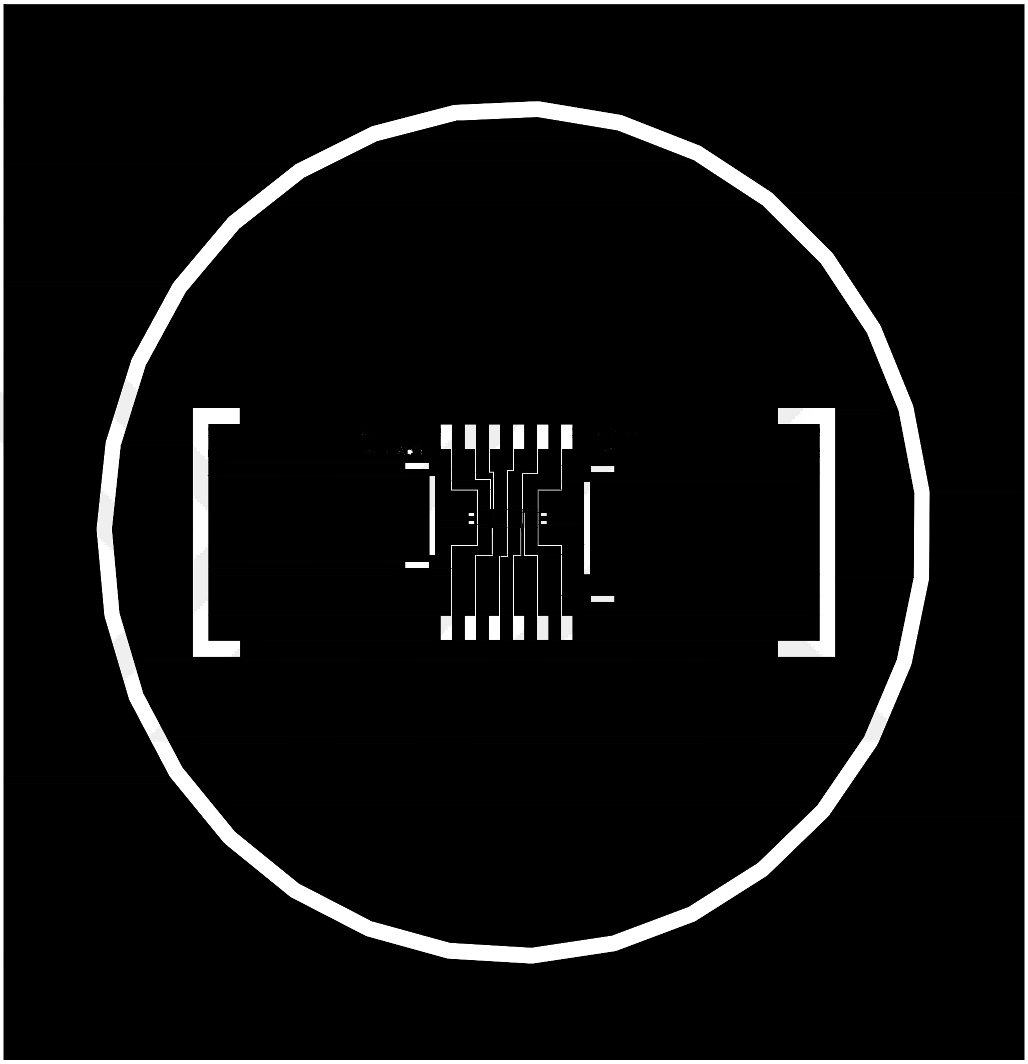

Figure B.2: Monodispersity evaluation chip electrode mask.

Appendix C

iDM Code

Due to the graphical essence of the LabVIEW, program code consists of graphical blocks. LabVIEW code of the iDM is illustrated in Figure C.1.

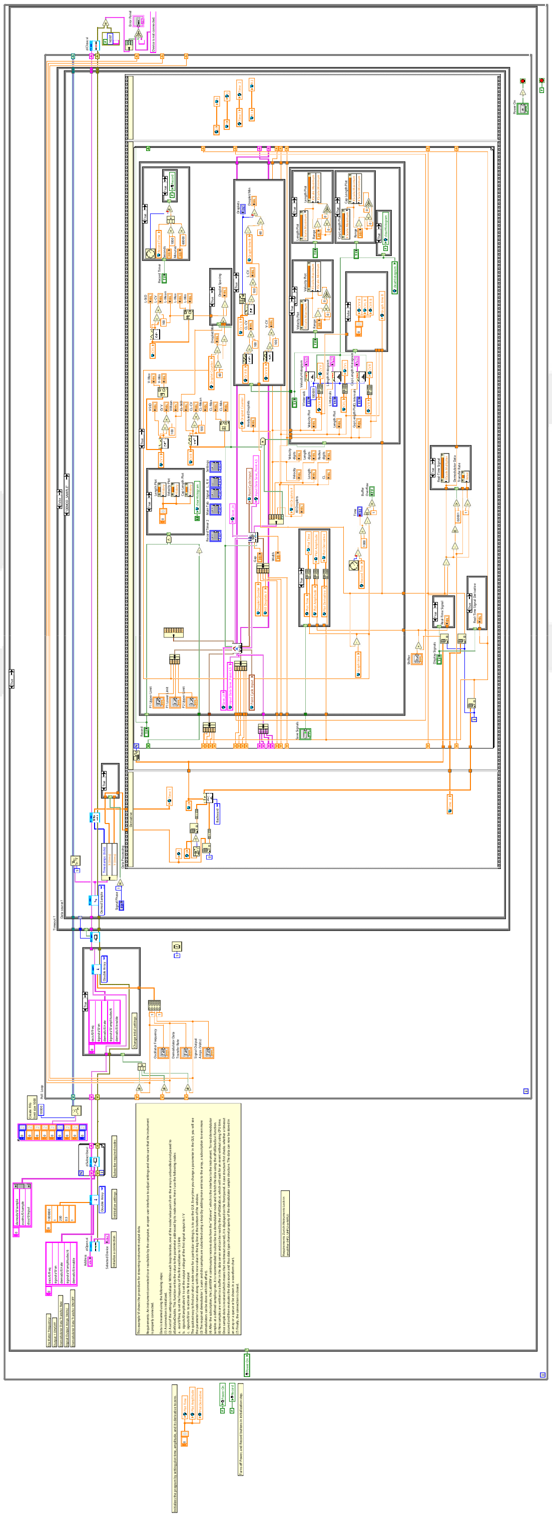

Figure C.1: iDM main block diagram.